Engineering Analysis with Boundary Elements 180 (2025) 106442

Contents lists available at ScienceDirect

Engineering Analysis with Boundary Elements

journal homepage: www.elsevier.com/locate/enganabound

A refined size-dependent modified strain gradient analysis of graphene platelet-reinforced functionally graded triply periodic minimal surface microplates using isogeometric analysis

P.T. Hung [a], M. Abdel-Wahab [b,c,d], P. Phung-Van [e], Chien H. Thai [f,g,*]

[a] Faculty of Civil Engineering, Ho Chi Minh City University of Technology and Education (HCMUTE), Ho Chi Minh City, Vietnam
[b] Soete Laboratory, Department of Electrical Energy, Metals, Mechanical Constructions and Systems, Faculty of Engineering and Architecture, Ghent University, Belgium
[c] College of Engineering, Yuan Ze University, Taiwan
[d] Parallel and Distributed Systems Laboratory, Jožef Stefan Institute, Jamova cesta 39, SI-1000, Ljubljana, Slovenija
[e] Faculty of Civil Engineering, HUTECH University, Ho Chi Minh City, Vietnam
[f] Mechanics of Advanced Materials and Structures, Institute for Advanced Study in Technology, Ton Duc Thang University, Ho Chi Minh City, Vietnam
[g] Faculty of Civil Engineering, Ton Duc Thang University, Ho Chi Minh City, Vietnam

ARTICLE INFO

Keywords:
Modified strain gradient theory
Refined plate theory
Functionally graded triply periodic minimal surface (FG-TPMS) microplate
Isogeometric analysis

ABSTRACT

In this study, a small scale dependence of graphene platelets reinforced functionally graded triply periodic minimal surface (GPR-FG-TPMS) microplates using an isogeometric analysis (IGA) is investigated. The research provides an in-depth analysis of three TPMS microplates, including Primitive (P), Gyroid (G) and I Wrapped Package (IWP) graph, along with two cellular solids, namely open and closed cell configurations. This study explores these designs under three graphene platelet distribution patterns and three distinct density distribution patterns. The governing equations are derived by integrating Hamilton's principle in conjunction with modified strain gradient theory (MSGT) based on refined plate theory within four variables. Leveraging continuous basis functions of the IGA, higher-order strains in MSGT and displacement fields are accurately captured. To validate proposed models, a comprehensive comparison between the obtained results and reference solutions is conducted. Furthermore, the influence of geometric configurations, density, length scale parameters (LSPs), GPLs distribution patterns and TPMS geometries on deflections and natural frequencies of the GPR-FG-TPMS microplates is comprehensively evaluated. The results indicate that increasing the LSPs enhances the natural frequencies and reduces the deflections of the microplates. The Primitive structure with a P-II density distribution exhibits the highest stiffness. Moreover, the GPL-A distribution provides superior mechanical performance compared to other patterns.

1. Introduction

To effectively model structural behaviors of microstructures, it is necessary to move beyond classical continuum mechanics because it fails to capture size dependence. Higher-order continuum theories, i.e., MSGT and modified couple stress theory (MCST), provide robust frameworks to address these shortcomings. Mindlin [1] introduced a general higher-order stress theory incorporating five LSPs to account for all components of strain gradients. The theory's complexity, however, stemming from its use of five LSPs and comprehensive strain gradient representation, limits its practical application. To simplify this approach, Lam et al. [2] introduced the MSGT, which reduced the complexity by incorporating only three LSPs. The MSGT has since been widely adopted in research on the mechanical behavior of microstructures. For example, Jamalpoor et al. [3] applied the MSGT to investigate the mechanical buckling behavior of double orthotropic Kirchhoff

* Corresponding author at: Mechanics of Advanced Materials and Structures, Institute for Advanced Study in Technology, Ton Duc Thang University, Ho Chi Minh City, Vietnam.
E-mail addresses: hungpht@hcmute.edu.vn (P.T. Hung), pv.phuc86@hutech.edu.vn (P. Phung-Van), thaihoangchien@tdtu.edu.vn (C.H. Thai).

https://doi.org/10.1016/j.enganabound.2025.106442
Received 9 June 2025; Received in revised form 13 August 2025; Accepted 31 August 2025
Available online 19 September 2025

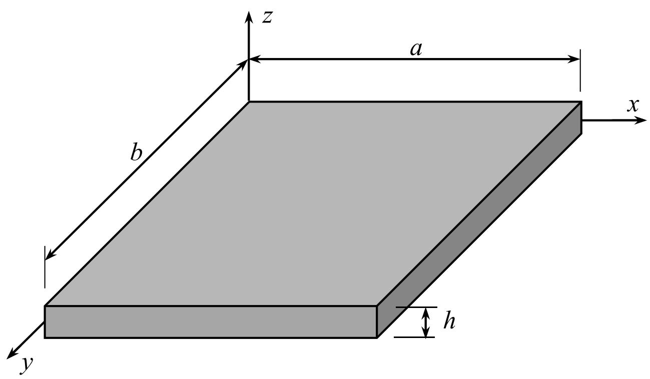

Fig. 1. The GPR-FG-TPMS rectangular microplate.

microplates under in-plane magnetic fields. Ashoori et al. [4] developed the first-order shear deformation plate theory (FSDT) and MSGT formulations for the nonlinear behavior of thick plates. Kandaz et al. [5] studied the bending of microbeams using the finite element method (FEM) based on both the MSGT and MCST. Furthermore, Gholami and Alizadeh [6] examined the bending of functionally graded (FG) microbeams on an elastic foundation using the MSGT and quasi-3D theory. Ansari et al. [7] studied thermal buckling and post-buckling behaviors of FG annular microplates using FSDT and MSGT. Based on the MSGT and refined plate theory (RPT), analytical solutions for size dependent effects of FG microplates supported by an elastic foundation were performed by Zhang et al. [8].

FG-TPMS materials represent an innovative class of metamaterials that combine the unique geometrical properties of TPMS structures with spatially varying material distributions. These materials are designed to optimize performance by seamlessly integrating high strength-to-weight ratios, exceptional energy absorption capabilities and functional adaptability. FG-TPMS materials are particularly suited for a wide range of advanced applications, including biomedical implants [9,10], robotics [11], absorption [12] and energy absorption systems [13–15]. The incorporation of functional grading into TPMS architecture allows for precise control over mechanical and physical properties, making it a promising solution for next-generation engineering challenges. In recent years, researchers have extensively focused on exploring the mechanical behavior of FG-TPMS structures. Employing both FEM and experimental method, Maskery et al. [16] examined the mechanical behaviors of TPMS structures under compressive loading. Employing the experimental and FEM, Simsek et al. [17] investigated dynamic responses of the Gyroid structures, while Abueidda et al. [18] examined the mechanical analysis of the TPMS structures, including Schwarz Primitive, Neovius and Schoen IWP cellular materials. Besides, Altintas et al. [19] focused on analyzing natural frequencies of the TPMS structures optimized for porous scaffolds. Kurup et al. [20] investigated the linear aeroelastic flutter of the Primitive, Gyroid, IWP and Diamond beams. In addition, the mechanical properties and energy absorption capacity of the printed Gyroid and Schwarz Primitive structures were studied by Yu et al. [21]. The findings revealed that the Primitive structure outperformed the Gyroid structures in energy absorption during compression tests, with the latter two exhibiting similar performance levels. Viet et al. [22] used FEM to find the critical buckling and natural frequencies of the Primitive, IWP, Gyroid and Diamond FG-TPMS beams. Zhang et al. [23] examined structural behaviors of FG-TPMS structures using the log-sigmoid method. Ejeh et al. [24] explored how relative density gradation and lattice hybridization affect the specific flexural properties of TPMS latticed beams. By evaluating different cubic porous topologies, the research identifies optimal structures for shear, uniaxial and combined loading. The results showed that the beams with functional grading and hybridization show significant improvements in flexural modulus and stiffness, with better crack resistance and reduced shear failure. Moreover, using a novel two-phase fitting method for relative density to determine the effective material properties, Nguyen-Xuan et al. [25] studied bending, free vibration and buckling analyses of the FG-TPMS plate.

GPLs are highly valued for their exceptional thermal and electrical conductivity and mechanical strength. They are used to improve composite materials, energy storage devices, and electronic and catalytic applications. Numerous studies on composite structures reinforced with GPLs have been conducted recently. Among these, Zhou et al. [26] used Donnell's shell theory and higher-order shear deformation theory (HSDT) to investigate the nonlinear stability of functionally graded porous (FGP) graphene platelet reinforced composite (GPLRC) cylindrical shells. Yang et al. [27] studied the buckling and post-buckling behaviors of the FG multilayer graphene platelet-reinforced beams using the FSDT and differential quadrature method (DQM). Wang et al. [28] utilized the Timoshenko beam theory and DQM to examine the forced vibration and nonlinear bending behaviors of the GPLRC beam with dielectric permittivity. Besides, studies on the static buckling and free vibration analyses of FGP GPLRC plate structures are available in Refs. [29–35]. In a related study on porous composite structures, Demir et al. [36] investigated the buckling of porous orthotropic laminated cylindrical panels under linearly varying edge compression using HSDT. Besides, Saffari et al. [37] studied the vibration of the FG-GPLRC nanoplates with magneto-electro-elastic facesheets and subjected to fluid environment based on the third-order shear deformation theory (TSDT), NSGT and IGA. Liang et al. [38] employed the TSDT and IGA to investigate the thermal buckling and vibration of the axial FGP-GPLRC arches resting on an elastic substrate. Tran et al. [39] studied GPR-FG TPMS plates using three grading frameworks: mass density, elastic modulus and shear modulus, and incorporating various porosity and GPL distributions. The HSDT with five variables and IGA were used to examine the static bending and free vibration of the GPR-FG-TPMS plates. The trigonometric shear deformation theory (TrSDT) and IGA were employed by Do et al. [40] to study the dynamic response of the GPR-FG-TPMS plates. In addition, Nam et al. [41] investigated the static, free vibration and dynamic instability analyses of the GPR-FG-TPMS nanoplates using the combination of the C^0-HSDT, nonlocal strain gradient theory (NSGT) and IGA. Pham et al. [42] utilized the HSDT, nonlocal elasticity theory and IGA to perform the forced vibration of the GPR-FG-TPMS nanoplates. It can be observed that micro-level behaviors of GPR-FG-TPMS structures have not yet been fully characterized.

IGA facilitates the achievement of any desired continuity level in the basis functions, ensuring the C^2-continuity required by the MSGT microplate model in its weak form. Thai et al. [43] introduced a size dependent model for the nonlinear analysis of functionally graded microplates. The proposed model was integrated three advanced theories: TSDT, MSGT, and IGA. In other words, a model integrated with RPT, MSGT and IGA was developed by Thai et al. [44] to study the bending, free vibration and buckling behaviors of isotropic and sandwich functionally graded microplates. Besides, Farzam et al. [45] employed this model to study free vibration and buckling of the FG microplates under thermal loading. Similarly, a combination of RPT, IGA and modified couple stress theory was introduced by Nam et al. [46] to investigate bending, buckling and free vibration of the FG-TPMS microplates. Unlike conventional FG-TPMS materials, adding GPLs significantly enhances stiffness, and intensifies sensitivity to LSPs due to their superior mechanical, thermal and electrical properties. These distinct material behaviors necessitate a dedicated investigation to capture the GPR-FG-TPMS structures' micro-scale responses accurately. Therefore, the present study proposes a novel computational framework integrating MSGT, RPT and IGA to analyze the size-dependent static bending and free vibration behaviors of GPR-FG-TPMS microplates. In addition, this work offers a comprehensive parametric study considering the combined effects of GPL weight fraction, GPL distribution patterns, mass density coefficients, cellular solid types and TPMS geometries. The existing literature has not reported such an extensive investigation on GPR-FG-TPMS microstructures at the microscale level. The findings from this study provide valuable insights into the design optimization of advanced lightweight, high-performance microscale plate structures and clarify how GPL reinforcement fundamentally alters their mechanical responses compared to conventional FG-TPMS counterparts.

2. The mathematical formulation

2.1. Material properties

In this study, a rectangular GPR-FG-TPMS microplate is considered, as illustrated in Fig. 1. The microplate incorporates three distinct sheet-based TPMS architectures, namely Gyroid, IWP and Primitive as shown in Fig. 2., combined with two types of cellular solid configurations: open-cell and closed-cell structures. The material properties are continuously graded along the plate thickness, influenced by both the GPL weight fraction and the porosity distribution. These FG-TPMS microstructures are constructed using the aforementioned unit cell geometries and are characterized by four primary mechanical parameters: shear modulus $G(z)$, mass density $\rho(z)$, Poisson's ratio $\nu(z)$ and elastic modulus $E(z)$. These properties are assumed to vary independently through the thickness direction according to the combined effects of material grading and porosity, following the relations presented in [25]

$$\begin{aligned}
&\text{Primitive}: \quad \frac{E(z)}{E_s} = \begin{cases} 0.317p^{1.264} & p \le 0.25 \\ 1.007p^{2.006} - 0.007 & p > 0.25 \end{cases} \\
&\qquad \frac{G(z)}{G_s} = \begin{cases} 0.705p^{1.189} & p \le 0.25 \\ 0.953p^{1.715} + 0.047 & p > 0.25 \end{cases} \\
&\qquad \nu(z) = \begin{cases} 0.314e^{-1.004p} + 0.119 & p \le 0.55 \\ 0.152p^2 - 0.235p + 0.383 & p > 0.55 \end{cases} \\
&\text{Gyroid}: \quad \frac{E(z)}{E_s} = \begin{cases} 0.596p^{1.467} & p \le 0.45 \\ 0.962p^{2.351} + 0.038 & p > 0.45 \end{cases} \\
&\qquad \frac{G(z)}{G_s} = \begin{cases} 0.777p^{1.544} & p \le 0.45 \\ 0.973p^{1.982} + 0.027 & p > 0.45 \end{cases} \\
&\qquad \nu(z) = \begin{cases} 0.192e^{-1.349p} + 0.202 & p \le 0.50 \\ 0.402p^2 - 0.603p + 0.501 & p > 0.50 \end{cases} \\
&\text{IWP}: \quad \frac{E(z)}{E_s} = \begin{cases} 0.597p^{1.225} & p \le 0.35 \\ 0.987p^{1.782} + 0.013 & p > 0.35 \end{cases} \\
&\qquad \frac{G(z)}{G_s} = \begin{cases} 0.529p^{1.287} & p \le 0.35 \\ 0.960p^{2.188} + 0.04 & p > 0.35 \end{cases} \\
&\qquad \nu(z) = \begin{cases} 2.597e^{-0.157p} - 2.244 & p \le 0.13 \\ 0.201p^2 - 0.227p + 0.326 & p > 0.13 \end{cases}
\end{aligned} \tag{1}$$

where E_s and G_s represent the elastic and shear modulus of the base material, respectively; p *is* the relative density expressed by

$$p = \frac{\rho(z)}{\rho_s} \tag{2}$$

in which ρ_s is the mass density of the base material.

This work examines various density distribution patterns, including symmetric (P-I), asymmetric (P-II) and uniform (P-III) distributions. The mass density grading function is generally defined as follows

$$\rho(z) = \rho_s p_{\max}[1 - p_0 + p_0\varphi(z)], p_0 = 1 - \frac{p_{\min}}{p_{\max}} \tag{3}$$

where $p_{\max}$ and $p_{\min}$ represent the maximum and minimum of relative density of the plate, respectively, while p_0 denotes the porosity coefficient. Besides, the function $\varphi(z)$ is defined as follows

$$\varphi(z) = \begin{cases} \left(\dfrac{z}{h} + \dfrac{1}{2}\right)^{n_I} & \text{P} - \text{I} \\ \left[1 - \cos\left(\dfrac{\pi z}{h}\right)\right]^{n_{II}} & \text{P} - \text{II} \\ \varphi_\rho & \text{P} - \text{III} \end{cases} \tag{4}$$

where n_I and n_{II} are the power index of the porosity density distributions I and II, respectively and φ_ρ denotes a coefficient of the porosity density distribution III. The coefficients n_I and $n_{II}$are defined as follows [39]

$$\begin{aligned}
&n_I = \frac{p_{\max}\rho_s h - M}{M - p_{\max}(1 - p_0)\rho_s h} \\
&\int_0^1 \frac{2}{\pi} \frac{p_{\max}[1 - p_0 + p_0(1-u)^{n_{II}}]}{\sqrt{1-u^2}} \mathrm{d}u = \frac{M}{\rho_s h} \\
&\varphi_\rho = \frac{\dfrac{M}{\rho_s h} - p_{\max}(1 - p_0)}{p_{\max}p_0}
\end{aligned} \tag{5}$$

where $u = \cos\left(\frac{\pi z}{h}\right)$; $M = \int_{-h/2}^{h/2} \rho(z)\mathrm{d}z$ is total mass per surface area.

According to Eq. (5), the relation between n_I, n_{II} and porosity distribution is determined from Table 1.

Two cellular architectures are used: closed-cell [47] for $0.15 < p < 1$ and open-cell [48]. The mechanical properties are described as follows

$$\text{Closed} - \text{cell} \begin{cases} \dfrac{E(z)}{E_s} = \left(\dfrac{p + 0.121}{1.121}\right)^{2.3} \\ G(z) = \dfrac{E(z)}{2(1+\nu(z))} \\ \nu(z) = 0.221(1-p) + \nu_s\left[0.342(1-p)^2 - 1.21(1-p) + 1\right] \end{cases}$$

$$\text{Open} - \text{cell}: \begin{cases} \dfrac{E(z)}{E_s} = p^2 \\ G(z) = \dfrac{E(z)}{2(1+\nu(z))} \\ \nu(z) = \dfrac{1}{3} \end{cases} \tag{6}$$

where ν_s denotes Poisson's ratio of the base material.

In this study, the base material of the FG-TPMS microplate is made of porous metallic material with various GPL distributions, characterized by the GPL volume fraction function $V_{GPL}(z)$, defined as

$$V_{GPL}(z) = \begin{cases} V_A\left(1 - \cos\left(\dfrac{\pi z}{h}\right)\right) & \text{GPL} - \text{A} \\ V_B\left[1 - \cos\left(\dfrac{\pi z}{2h} + \dfrac{\pi}{4}\right)\right] & \text{GPL} - \text{B} \\ V_C & \text{GPL} - \text{C} \end{cases} \tag{7}$$

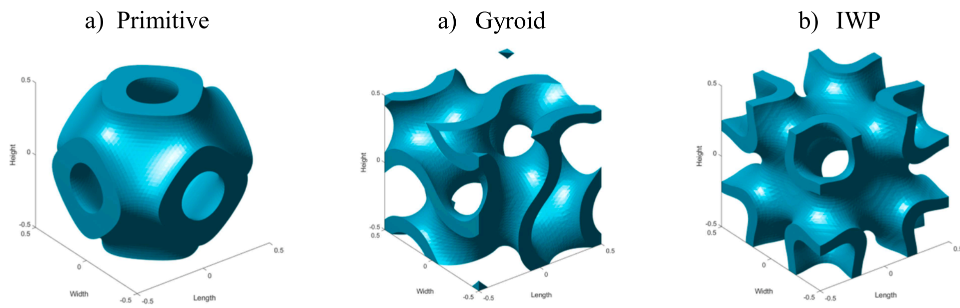

Fig. 2. The Primitive, Gyroid and IWP FG-TPMS unit cells [52].

Table 1
The coefficients $n_I$and $n_{II}$with various density porosity coefficient (P_{max}=1, $M/(\rho_s h) = 0.35$).

p_0	n_I	n_{II}
0.40	−2.6000	30.3062
0.45	−3.2450	29.8452
0.50	−4.3333	29.3236
0.60	−12.9999	27.7595
0.70	13.0000	7.9991
0.75	6.5000	3.9120
0.80	4.3333	2.5669
0.85	3.2500	1.9024
0.90	2.6000	1.5078
0.95	2.1666	1.2471

where V_k ($k = A, B, C$) represents the maximum GPL volume fraction, which are formulated as

$$\frac{W_{GPL}\rho_m}{W_{GPL}\rho_m + \rho_{GPL}(1 - W_{GPL})}\int_{-h/2}^{h/2}\frac{\rho(z)}{\rho_s}dz = \begin{cases} V_A\displaystyle\int_{-h/2}^{h/2}\frac{\rho(z)}{\rho_s}\left(1-\cos\left(\frac{\pi z}{h}\right)\right)dz \\ V_B\displaystyle\int_{-h/2}^{h/2}\frac{\rho(z)}{\rho_s}\left[1-\cos\left(\frac{\pi z}{2h}+\frac{\pi}{4}\right)\right]dz \\ V_C\displaystyle\int_{-h/2}^{h/2}\frac{\rho(z)}{\rho_s}dz \end{cases} \tag{8}$$

where W_{GPL} and $\rho_{GPL}$are the GPLs weight fraction and mass density respectively and $\rho_m$is mass density of the metal.

The elastic modulus of the base material E_s is calculated using the Halpin-Tsai micromechanical model [49,50]

$$E_s = \frac{E_m}{8}\left[3\frac{1+\zeta_L\eta_L V_{GPL}(z)}{1-\eta_L V_{GPL}(z)} + 5\frac{1+\zeta_W\eta_W V_{GPL}(z)}{1-\eta_W V_{GPL}(z)}\right] \tag{9}$$

with

$$\eta_L = \frac{E_{GPL}-E_m}{E_{GPL}+E_m\zeta_L};\ \eta_W = \frac{E_{GPL}-E_m}{E_{GPL}+E_m\zeta_W};\ \zeta_L = \frac{2l_{GPL}}{t_{GPL}};\ \zeta_W = \frac{2w_{GPL}}{t_{GPL}} \tag{10}$$

where E_m and E_{GPL} are the elastic modulus of the matrix and GPLs, respectively and w_{GPL}, l_{GPL} and t_{GPL} represent the average width, length and thickness of the GPLs, respectively.

According to the rule of mixture [51], the Poisson's ratio and mass density of the base material are expressed

$$\begin{cases} \rho_s = \rho_m(1-V_{GPL}(z)) + \rho_{GPL}V_{GPL}(z) \\ \nu_s = \nu_m(1-V_{GPL}(z)) + \nu_{GPL}V_{GPL}(z) \end{cases} \tag{11}$$

where ν_m and ν_{GPL} represent the Poisson's ratio of the matrix and GPLs, respectively.

2.2. Kinematics of the GPR-FG-TPMS microplate

The refined plate theory with four variables [53] is employed in this study with the following assumption:

- The displacements are assumed to be small compared to the plate thickness, resulting in infinitesimal strains and allowing the application of linear strain-displacement relations throughout the analysis.
- The transverse normal stress σ_z is considered negligible relative to the in-plane normal stresses σ_x and σ_y, which is acceptable for thin and moderately thick plates subjected to bending and transverse loading.
- A predefined shape function approximates the transverse shear strain distribution across thickness, which may affect accuracy for thick microplates.
- The total transverse displacement $\hat{w}(x, y, z)$ is expressed as the sum of a bending displacement $w_b(x,y)$ and a shear displacement $w_s(x,y)$.
- The in-plane displacements in the x- and y-directions, denoted as $\hat{u}$ and $\hat{v}$, respectively, are expressed as follows

$$\begin{aligned} \hat{u}(x,y,z) &= u(x,y) - zw_{b,x}(x,y) + f(z)w_{s,x}(x,y) \\ \hat{v}(x,y,z) &= u(x,y) - zw_{b,y}(x,y) + f(z)w_{s,y}(x,y) \end{aligned} \tag{12}$$

in which symbols ",x" and ",y" indicate derivatives with respect to x and y, respectively, and u and v represent displacements of the middle-plane in the x- and y-directions, respectively.

Based on the aforementioned assumptions, the refined plate theory achieves computational efficiency by reducing the variable count by one compared to higher-order shear deformation theory. This formulation provides an optimal balance between computational efficiency and analytical precision for thin to moderately thick plate structures, as it incorporates both bending and shear strain effects without requiring shear correction factors. However, the theory exhibits several inherent limitations. The formulation cannot adequately represent complex through-thickness displacement variations, which becomes critically important for very thick plates where warping phenomena are pronounced. The theory is neglect of transverse normal stress further compounds this limitation. Additionally, implementing fully clamped boundary conditions presents challenges due to the theory is incorporation of derivatives from both bending and shear displacement components.

In the present investigation, these boundary condition enforcement difficulties are addressed through the superior continuity properties of NURBS basis functions within the isogeometric analysis framework. The higher-order continuity inherent in NURBS enables direct enforcement of derivatives for both bending and shear displacements by constraining the transverse bending and shear displacements to zero at control points and neighboring control points, thereby circumventing traditional implementation challenges associated with clamped boundary condi-

Table 2
Material properties of the base material and GPLs.

Type	E (GPa)	ν	ρ (kg/m^3)
Steel	200	0.3	8000
GPLs	1010	0.186	10,620

tions. The displacement fields of the GPR-FG-TPMS microplate based on the above assumption, can be formulated as follows

$$\mathbf{u} = \mathbf{u}_1 + z\mathbf{u}_2 + f(z)\mathbf{u}_3 \tag{13}$$

where

$$\mathbf{u} = \begin{Bmatrix} \widehat{u}(x,y,z) \\ \widehat{v}(x,y,z) \\ \widehat{w}(x,y,z) \end{Bmatrix}; \mathbf{u}_1 = \begin{Bmatrix} u(x,y) \\ v(x,y) \\ w_b(x,y) + w_s(x,y) \end{Bmatrix}; \mathbf{u}_2 = \begin{Bmatrix} -w_{b,x}(x,y) \\ -w_{b,y}(x,y) \\ 0 \end{Bmatrix}; \mathbf{u}_3 = \begin{Bmatrix} w_{s,x}(x,y) \\ w_{s,y}(x,y) \\ 0 \end{Bmatrix}; f(z) = -4z^3 \Big/ 3h^2 \tag{14}$$

The strain is given as

$$\boldsymbol{\varepsilon} = \begin{Bmatrix} \boldsymbol{\varepsilon}_b \\ \boldsymbol{\varepsilon}_s \end{Bmatrix} = \begin{Bmatrix} \boldsymbol{\varepsilon}_{b1} + z\boldsymbol{\varepsilon}_{b2} + f(z)\boldsymbol{\varepsilon}_{b3} \\ [1 + f'(z)]\boldsymbol{\gamma}_s \end{Bmatrix} \tag{15}$$

where$f'(z) = \frac{df(z)}{dz}$ is the derivate of the function $f(z)$.

The relation between the stress and the strain of the microplate is given

$$\begin{cases} \boldsymbol{\sigma}_b = \mathbf{C}_b\boldsymbol{\varepsilon}_b \\ \boldsymbol{\sigma}_s = \mathbf{C}_s\boldsymbol{\varepsilon}_s \end{cases} \tag{16}$$

where

$$\boldsymbol{\sigma}_b = \begin{Bmatrix} \sigma_x \\ \sigma_y \\ \tau_{xy} \end{Bmatrix}; \boldsymbol{\sigma}_s = \begin{Bmatrix} \tau_{xz} \\ \tau_{yz} \end{Bmatrix}; \mathbf{C}_b = \begin{bmatrix} c_{11} & c_{12} & 0 \\ c_{12} & c_{22} & 0 \\ 0 & 0 & c_{66} \end{bmatrix}; \mathbf{C}_s = \begin{bmatrix} c_{55} & 0 \\ 0 & c_{44} \end{bmatrix} \tag{17}$$

where σ_x, σ_y, τ_{xy}, τ_{xz} and τ_{yz} correspond to the components of the stress tensor, and

$$c_{11} = c_{22} = \frac{E(1-\nu)}{(1+\nu)(1-2\nu)}; \; c_{12} = \frac{E\nu}{(1+\nu)(1-2\nu)}; \; c_{44} = c_{55} = c_{66} = \frac{E}{2(1+\nu)} \tag{18}$$

Based on the MSGT presented in [54], which incorporates size-dependent effects via the rotation gradient tensor, the following formulation is derived

$$\boldsymbol{\chi} = \frac{1}{2}\left[\boldsymbol{\theta} + (\nabla\boldsymbol{\theta})^T\right]$$

with

$$\boldsymbol{\theta} = \nabla \times \mathbf{u} = \frac{1}{2}\left\{ \widehat{w}_{,y} - \widehat{v}_{,z} \quad \widehat{u}_{,z} - \widehat{v}_{,x} \quad \widehat{v}_{,x} - \widehat{u}_{,y} \right\}^T \tag{19}$$

where $\boldsymbol{\chi}$ denotes the rotation gradient tensor. By substituting the displacements from Eq. (13) into Eq. (19), the tensor $\boldsymbol{\chi}$ is given

$$\begin{aligned} \boldsymbol{\chi} = \{\boldsymbol{\chi}_b \quad \boldsymbol{\chi}_s\}^T; \; \boldsymbol{\chi}_b = \{\chi_{xx} \quad \chi_{yy} \quad \chi_{xy}\}^T = \boldsymbol{\chi}_{b1} + f'(z)\boldsymbol{\chi}_{b2} \\ \boldsymbol{\chi}_s = \{\chi_{xz} \quad \chi_{yz}\}^T = \boldsymbol{\chi}_{s1} + f''(z)\boldsymbol{\chi}_{s2} \end{aligned} \tag{20}$$

The dilatation gradient tensor employing the MSGT [54], takes the form

Table 3
The first dimensionless frequency of the SSSS FG-TPMS square plate ($l_0 = 0$).

a/h	p_0	TPMS	P-I		P-II		P-III	
			IGA	Ref. [39]	IGA	Ref. [39]	IGA	Ref. [39]
10	0.75	P	3.7054	3.7051	4.1931	4.1936	3.5511	3.5512
		G	3.6616	3.6608	4.0872	4.0872	3.4735	3.4736
		IWP	3.7611	3.7602	4.1466	4.1469	3.5338	3.5340
		Closed-cell	3.5967	3.5957	4.0795	4.0794	3.4258	3.4259
		Open-cell	3.4921	3.4906	4.0539	4.0528	3.3760	3.3761
	0.85	P	3.4546	3.4543	4.3954	4.3894	3.5511	3.5512
		G	3.3621	3.3614	4.2616	4.2496	3.4735	3.4736
		IWP	3.5150	3.5139	4.3150	4.3042	3.5338	3.5340
		Closed-cell	3.3056	3.3047	4.2617	4.2486	3.4258	3.4259
		Open-cell	3.0919	3.0911	4.2072	4.1823	3.3760	3.3761
	0.95	P	3.1584	3.1584	4.4812	4.4619	3.5511	3.5512
		G	3.0433	3.0432	4.3448	4.3135	3.4735	3.4736
		IWP	3.2080	3.2076	4.3883	4.3584	3.5338	3.5340
		Closed-cell	3.0711	3.0709	4.3582	4.3285	3.4258	3.4259
		Open-cell	2.8203	2.8202	4.3033	4.2538	3.3760	3.3761
200	0.75	P	3.7735	3.7735	4.3172	4.3172	3.6008	3.6008
		G	3.7455	3.7455	4.2408	4.2408	3.5300	3.5300
		IWP	3.8602	3.8602	4.3184	4.3184	3.6003	3.6003
		Closed-cell	3.6806	3.6806	4.2462	4.2462	3.4827	3.4827
		Open-cell	3.5809	3.5809	4.2606	4.2606	3.4372	3.4372
	0.85	P	3.5010	3.5010	4.5947	4.5946	3.6008	3.6008
		G	3.4141	3.4141	4.5165	4.5165	3.5300	3.5300
		IWP	3.5802	3.5802	4.5871	4.5871	3.6003	3.6003
		Closed-cell	3.3563	3.3563	4.5328	4.5327	3.4827	3.4827
		Open-cell	3.1362	3.1362	4.5605	4.5604	3.4372	3.4372
	0.95	P	3.1848	3.1848	4.7439	4.7438	3.6008	3.6008
		G	3.0707	3.0707	4.6687	4.6686	3.5300	3.5300
		IWP	3.2436	3.2436	4.7344	4.7343	3.6003	3.6003
		Closed-cell	3.1003	3.1003	4.6884	4.6883	3.4827	3.4827
		Open-cell	2.8428	2.8428	4.7219	4.7217	3.4372	3.4372

Table 4
The normalized central deflection of the SSSS FG-TPMS square plate ($l_0 = 0$).

a/h	p_0	TPMS	P-I		P-II		P-III	
			IGA	Ref. [39]	IGA	Ref. [39]	IGA	Ref. [39]
10	0.75	P	2.3359	2.3354	1.4226	1.4233	2.7814	2.7819
		G	2.4597	2.4575	1.5761	1.5760	3.0453	3.0457
		IWP	2.2126	2.2104	1.4881	1.4884	2.8472	2.8476
		Closed-cell	2.6430	2.6403	1.5883	1.5880	3.2218	3.2221
		Open-cell	2.9721	2.9674	1.6279	1.6262	3.4150	3.4154
	0.85	P	3.1043	3.1033	1.1801	1.1739	2.7814	2.7819
		G	3.4752	3.4722	1.3413	1.3266	3.0453	3.0457
		IWP	2.9143	2.9107	1.2750	1.2626	2.8472	2.8476
		Closed-cell	3.7211	3.7175	1.3424	1.3264	3.2218	3.2221
		Open-cell	4.8574	4.8526	1.4255	1.3931	3.4150	3.4154
	0.95	P	4.4689	4.4691	1.1019	1.0835	2.7814	2.7819
		G	5.2034	5.2024	1.2593	1.2244	3.0453	3.0457
		IWP	4.2215	4.2196	1.2084	1.1766	2.8472	2.8476
		Closed-cell	5.0207	5.0192	1.2421	1.2095	3.2218	3.2221
		Open-cell	7.0562	7.0556	1.3279	1.2694	3.4150	3.4154
200	0.75	P	2.2201	2.2201	1.3007	1.3008	2.6801	2.6801
		G	2.2971	2.2971	1.3986	1.3987	2.9101	2.9101
		IWP	2.0397	2.0397	1.3026	1.3027	2.6956	2.6956
		Closed-cell	2.4655	2.4655	1.3925	1.3925	3.0748	3.0748
		Open-cell	2.7519	2.7519	1.3741	1.3742	3.2410	3.2410
	0.85	P	2.9953	2.9953	1.0149	1.0148	2.6801	2.6801
		G	3.3273	3.3272	1.0882	1.0880	2.9101	2.9101
		IWP	2.7562	2.7562	1.0239	1.0237	2.6956	2.6956
		Closed-cell	3.5650	3.5650	1.0733	1.0731	3.0748	3.0748
		Open-cell	4.6761	4.6761	1.0483	1.0480	3.2410	3.2410
	0.95	P	4.3761	4.3761	0.8938	0.8936	2.6801	2.6801
		G	5.0843	5.0842	0.9538	0.9535	2.9101	2.9101
		IWP	4.0906	4.0906	0.9029	0.9026	2.6951	2.6956
		Closed-cell	4.8962	4.8962	0.9383	0.9380	3.0748	3.0748
		Open-cell	6.9254	6.9254	0.9129	0.9123	3.2410	3.2410

$$\boldsymbol{\xi} = \begin{Bmatrix} \xi_x \\ \xi_y \\ \xi_z \end{Bmatrix} = \begin{Bmatrix} \varepsilon_{xx,x} + \varepsilon_{yy,x} + \varepsilon_{zz,x} \\ \varepsilon_{xx,y} + \varepsilon_{yy,y} + \varepsilon_{zz,y} \\ \varepsilon_{xx,z} + \varepsilon_{yy,z} + \varepsilon_{zz,z} \end{Bmatrix} = \boldsymbol{\xi}_1 + z\boldsymbol{\xi}_2 + f(z)\boldsymbol{\xi}_3 + f'(z)\boldsymbol{\xi}_4 \tag{21}$$

where $\boldsymbol{\xi}$ is the dilatation gradient tensor.

Similarly, the tensor of deviatoric stretch gradient ($\boldsymbol{\eta}$) is defined

$$\begin{aligned} &\boldsymbol{\eta} = \{\boldsymbol{\eta}_b \ \ \boldsymbol{\eta}_s\}^T \\ &\boldsymbol{\eta}_b = \{\eta_{xxx} \ \ \eta_{yyy} \ \ \eta_{yyx} \ \ \eta_{xxy} \ \ \eta_{zzx} \ \ \eta_{zzy}\}^T = \boldsymbol{\eta}_{b1} + z\boldsymbol{\eta}_{b2} + f(z)\boldsymbol{\eta}_{b3} + f''(z)\boldsymbol{\eta}_{b4} \\ &\boldsymbol{\eta}_s = \{\eta_{zzz} \ \ \eta_{xxz} \ \ \eta_{yyz} \ \ \eta_{xyz}\}^T = \boldsymbol{\eta}_{s1} + f'(z)\boldsymbol{\eta}_{s2} \end{aligned} \tag{22}$$

The relation between the higher-order stresses and strains using the MSGT model [54] is expressed as follows

$$\begin{cases} \mathbf{m}_b = 2\mu l_1^2 \mathbf{I}_{3\times3}\boldsymbol{\chi}_b \\ \mathbf{m}_s = 2\mu l_1^2 \mathbf{I}_{2\times2}\boldsymbol{\chi}_s \end{cases} \tag{23}$$

$$\mathbf{p} = 2\mu l_2^2 \mathbf{I}_{3\times3}\boldsymbol{\xi} \tag{24}$$

$$\begin{cases} \widehat{\boldsymbol{\tau}}_b = 2\mu l_3^2 \mathbf{I}_{6\times6}\boldsymbol{\eta}_b \\ \widehat{\boldsymbol{\tau}}_s = 2\mu l_3^2 \mathbf{I}_{4\times4}\boldsymbol{\eta}_s \end{cases} \tag{25}$$

in which $\mu = G$ is Lame's coefficient; $l_i (i = 1, 2, 3)$ denote three LSPs; $\mathbf{I}_{2\times2}$, $\mathbf{I}_{3\times3}$, $\mathbf{I}_{4\times4}$ and $\mathbf{I}_{6\times6}$ represent the 2 × 2, 3 × 3, 4 × 4 and 6 × 6 identity matrices, respectively, and

$$\begin{aligned} &\mathbf{m}_b = \{m_{xx} \ \ m_{yy} \ \ m_{xy}\}^T; \ \mathbf{m}_s = \{m_{xz} \ \ m_{yz}\}^T; \ \mathbf{p} = \{p_x \ \ p_y \ \ p_z\}^T \\ &\widehat{\boldsymbol{\tau}}_b = \{\widehat{\tau}_{xxx} \ \ \widehat{\tau}_{yyy} \ \ \widehat{\tau}_{yyx} \ \ \widehat{\tau}_{xxy} \ \ \widehat{\tau}_{zzx} \ \ \widehat{\tau}_{zzy}\}^T; \ \widehat{\boldsymbol{\tau}}_s = \{\widehat{\tau}_{zzz} \ \ \widehat{\tau}_{xxz} \ \ \widehat{\tau}_{yyz} \ \ \widehat{\tau}_{xyz}\}^T \end{aligned} \tag{26}$$

2.3. The variational principle

The formulation of Hamilton's principle for the microplate can be expressed

$$\int_0^t (\delta U - \delta T - \delta W)\mathrm{d}t = 0 \tag{27}$$

where δT, δU and δW respectively correspond to the virtual kinetic energy, strain energy and work done by the external load.

Using the MSGT model [54], the virtual strain energy is formulated

$$\delta U = \int_V \left(\delta\boldsymbol{\varepsilon}_b^T\boldsymbol{\sigma}_b + \delta\boldsymbol{\varepsilon}_s^T\boldsymbol{\sigma}_s + \delta\boldsymbol{\chi}_b^T\mathbf{m}_b + \delta\boldsymbol{\chi}_s^T\mathbf{m}_s + \delta\boldsymbol{\xi}^T\mathbf{p} + \delta\boldsymbol{\eta}_b^T\widehat{\boldsymbol{\tau}}_b + \delta\boldsymbol{\eta}_s^T\widehat{\boldsymbol{\tau}}_s\right)\mathrm{d}V \tag{28}$$

in which the volume of the body is denoted by V.

Substituting Eqs. (16), (23), (24), and (25) into Eq. (28), we obtain

$$\begin{aligned} \delta U = &\int_\Omega \delta(\overline{\boldsymbol{\varepsilon}}_b)^T\overline{\mathbf{C}}_u\overline{\boldsymbol{\varepsilon}}_b\mathrm{d}\Omega + \int_\Omega \delta(\boldsymbol{\gamma}_s)^T\overline{\mathbf{C}}_s\boldsymbol{\gamma}_s\mathrm{d}\Omega + \int_\Omega \delta(\overline{\boldsymbol{\chi}}_b)^T\overline{\mathbf{C}}_{rb}\overline{\Gamma}_{rb}\overline{\boldsymbol{\chi}}_b\mathrm{d}\Omega + \int_\Omega \delta(\overline{\boldsymbol{\chi}}_s)^T\overline{\mathbf{C}}_{rs}\overline{\Gamma}_{rs}\overline{\boldsymbol{\chi}}_s\mathrm{d}\Omega \\ &+ \int_\Omega \delta\overline{\boldsymbol{\xi}}^T\overline{\mathbf{C}}_{dil}\overline{\boldsymbol{\xi}}\mathrm{d}\Omega + \int_\Omega \delta(\overline{\boldsymbol{\eta}}_b)^T\overline{\mathbf{C}}_{deb}\overline{\Gamma}_{deb}\overline{\boldsymbol{\eta}}_b\mathrm{d}\Omega + \int_\Omega \delta(\overline{\boldsymbol{\eta}}_s)^T\overline{\mathbf{C}}_{des}\overline{\Gamma}_{des}\overline{\boldsymbol{\eta}}_s\mathrm{d}\Omega \end{aligned} \tag{29}$$

Table 5
The lowest six frequencies of the SSSS GPR-FG-TPMS square microplate ($a = 10h$, GPL-A, $p_0 = 0.7$, $W_{GPL} = 0.01$).

Porosity distribution	l_0/h	Mode	TPMS				
			P	G	IWP	Closed-cell	Open-Cell
P-I	0	1	4.2075	4.1277	4.2088	4.0668	4.0016
		2	6.3525	6.2779	6.4255	6.2052	6.0811
		3	6.3525	6.2779	6.4255	6.2052	6.0811
		4	7.9703	7.7427	7.8328	7.6145	7.4399
		5	8.5382	8.4512	8.6407	8.3625	8.1576
		6	8.5382	8.4512	8.6407	8.3625	8.1576
	0.2	1	4.7545	4.6032	4.6429	4.5349	4.4388
		2	7.2813	7.0848	7.1661	6.9977	6.8361
		3	7.2957	7.1030	7.1884	7.0167	6.8571
		4	9.1569	8.8260	8.8591	8.6916	8.4810
		5	9.9424	9.6846	9.7887	9.5768	9.3344
		6	9.9838	9.7383	9.8543	9.6332	9.3960
	0.4	1	5.7598	5.5029	5.4842	5.4186	5.2684
		2	8.9219	8.5536	8.5407	8.4360	8.1983
		3	8.9462	8.5787	8.5687	8.4607	8.2227
		4	11.2293	10.7229	10.6663	10.5601	10.2588
		5	12.3158	11.8315	11.8151	11.6799	11.3440
		6	12.3871	11.9079	11.9016	11.7556	11.4184
	0.6	1	6.7545	6.4144	6.3552	6.3141	6.1183
		2	10.5029	10.0083	9.9297	9.8620	9.5560
		3	10.5321	10.0356	9.9584	9.8880	9.5801
		4	13.2247	12.5692	12.4459	12.3746	11.9878
		5	14.6064	13.9043	13.8087	13.7076	13.2806
		6	14.6937	13.9882	13.8945	13.7882	13.3547
P-II	0	1	4.4658	4.3570	4.4222	4.3317	4.3132
		2	6.7664	6.5936	6.7034	6.5616	6.4887
		3	6.7664	6.5936	6.7034	6.5616	6.4887
		4	8.3844	8.0881	8.1420	8.0089	7.8816
		5	9.0943	8.8222	8.9472	8.7701	8.6087
		6	9.0943	8.8222	8.9472	8.7701	8.6087
	0.2	1	4.9518	4.7911	4.8255	4.7544	4.7077
		2	7.6025	7.3604	7.4260	7.3155	7.2206
		3	7.6211	7.3833	7.4531	7.3402	7.2499
		4	9.5030	9.1543	9.1721	9.0728	8.9390
		5	10.3849	10.0386	10.1114	9.9786	9.8129
		6	10.4391	10.1052	10.1907	10.0510	9.8971
	0.4	1	5.8867	5.6322	5.6146	5.5705	5.4604
		2	9.1446	8.7644	8.7494	8.6814	8.5053
		3	9.1705	8.7904	8.7788	8.7076	8.5325
		4	11.4921	10.9976	10.9381	10.8805	10.6571
		5	12.6585	12.1427	12.1161	12.0379	11.7856
		6	12.7374	12.2232	12.2075	12.1197	11.8705
	0.6	1	6.8445	6.5097	6.4522	6.4258	6.2606
		2	10.6849	10.1821	10.1028	10.0636	9.8083
		3	10.7130	10.2072	10.1295	10.0876	9.8311
		4	13.4496	12.8145	13.1388	12.6595	12.3416
		5	14.8699	14.1957	14.0848	14.0443	13.6947
		6	14.9584	14.2760	14.1712	14.1222	13.7689
P-III	0	1	3.9888	3.8983	3.9626	3.8377	3.7829
		2	6.0549	5.9711	6.1139	5.9104	5.8122
		3	6.0549	5.9711	6.1139	5.9104	5.8122
		4	7.6462	7.4258	7.4967	7.3045	7.1696
		5	8.1868	8.1111	8.3187	8.0531	7.8961
		6	8.1868	8.1111	8.3187	8.0531	7.8961
	0.2	1	4.5586	4.3706	4.3740	4.2928	4.1896
		2	6.9959	6.7324	6.7643	6.6338	6.4616
		3	7.0059	6.7439	6.7781	6.6456	6.4741
		4	8.7999	8.3951	8.3564	8.2399	8.0145
		5	9.5691	9.2119	9.2530	9.0900	8.8324
		6	9.5988	9.2465	9.2949	9.1258	8.8699
	0.4	1	5.5765	5.2615	5.1874	5.1572	4.9856
		2	8.6210	8.1422	8.0399	7.9917	7.7165
		3	8.6480	8.1703	8.0708	8.0200	7.7453
		4	10.8172	10.1783	10.0044	9.9717	9.6207
		5	11.8693	11.2019	11.0530	10.9995	10.6051
		6	11.9498	11.2861	11.1460	11.0846	10.6911
	0.6	1	6.5658	6.1552	6.0284	6.0279	5.8029
		2	10.1750	9.5421	9.3523	9.3508	8.9952
		3	10.2163	9.5831	9.3951	9.3916	9.0358
		4	12.7577	11.9415	11.6751	11.6902	11.2406
		5	14.0344	13.1538	12.8853	12.8916	12.3903
		6	14.1579	13.2765	13.0137	13.0140	12.5116

Table 6
The lowest six frequencies of the CCCC GPR-FG-TPMS square microplate (GPL-A case, $a = 10h$, $p_0 = 0.7$, $W_{GPL} = 0.01$).

Porosity distribution	l_0/h	Mode	TPMS				
			P	G	IWP	Closed-cell	Open-Cell
P-I	0	1	5.3652	5.3162	5.4516	5.2637	5.1512
		2	7.4141	7.3111	7.4619	7.2305	7.0499
		3	7.4141	7.3111	7.4619	7.2305	7.0499
		4	8.8901	8.6478	8.7477	8.5195	8.2864
		5	9.4394	9.2533	9.3897	9.1387	8.8704
		6	9.4914	9.3290	9.4826	9.2196	8.9548
	0.2	1	6.2074	6.0491	6.1285	5.9833	5.8436
		2	8.6608	8.4141	8.4935	8.3180	8.1072
		3	8.6901	8.4512	8.5382	8.3569	8.1496
		4	10.4382	10.0695	10.1045	9.9324	9.6719
		5	11.2235	10.8722	10.9312	10.7443	10.4492
		6	11.2983	10.9689	11.0477	10.8455	10.5568
	0.4	1	7.6534	7.3410	7.3365	7.2462	7.0429
		2	10.7576	10.3134	10.3108	10.1839	9.8999
		3	10.8097	10.3670	10.3595	10.2366	9.9503
		4	12.9943	12.4329	12.2947	12.2731	11.7856
		5	14.1133	13.4799	12.4123	13.3160	11.9400
		6	14.2300	13.6153	13.3999	13.4534	12.9319
	0.6	1	9.0357	8.6062	8.5425	8.4851	8.2239
		2	12.7317	12.1325	12.0347	11.9649	11.5970
		3	12.7969	12.1928	12.0984	12.0230	11.6511
		4	15.3831	14.6475	14.5102	14.4377	13.9909
		5	16.7427	15.9543	15.8290	15.7478	15.2630
		6	16.8958	16.0021	15.9594	15.8509	15.3346
P-II	0	1	5.7178	5.5719	5.6706	5.5480	5.4719
		2	7.8704	7.6217	7.7189	7.5710	7.4239
		3	7.8704	7.6217	7.7189	7.5710	7.4239
		4	9.3441	8.9752	9.0232	8.8820	8.6773
		5	9.9721	9.5827	9.6509	9.4924	9.2488
		6	10.0475	9.6718	9.7529	9.5873	9.3470
	0.2	1	6.4825	6.2820	6.3458	6.2493	6.1635
		2	9.0263	8.7181	8.7722	8.6625	8.5153
		3	9.0638	8.7637	8.8258	8.7118	8.5723
		4	10.8309	10.4207	10.4304	10.3327	10.1433
		5	11.67478	11.2366	11.2582	11.1516	10.9237
		6	11.77349	11.3529	11.3936	11.2765	11.0629
	0.4	1	7.8452	7.5250	7.5184	7.4586	7.3062
		2	11.0337	10.5810	10.5500	10.4875	10.2659
		3	11.0893	10.6377	10.6137	10.5450	10.3256
		4	13.3239	12.7637	12.6900	12.6401	12.3705
		5	14.4690	13.8733	13.8012	13.7512	13.4493
		6	14.6051	14.0121	13.9561	13.8927	13.5954
	0.6	1	9.1876	8.7613	8.6975	8.6633	8.4443
		2	12.9756	12.3877	12.2851	12.2550	11.9501
		3	13.0389	12.4455	12.3468	12.3112	12.0040
		4	15.7004	14.9892	14.8413	14.8244	14.4590
		5	17.1066	16.3543	16.2007	16.1888	15.7936
		6	17.2634	16.4995	16.3552	16.3312	15.9309
P-III	0	1	5.1041	5.0629	5.2044	5.0258	4.9375
		2	7.0984	7.0202	7.1874	6.9656	6.8269
		3	7.0984	7.0202	7.1874	6.9656	6.8269
		4	8.5707	8.3638	8.4675	8.2577	8.0795
		5	9.1112	8.9800	9.1459	8.9066	8.7001
		6	9.1476	9.0354	9.2219	8.9680	8.7655
	0.2	1	5.9487	5.7379	5.7779	5.6629	5.5121
		2	8.3155	7.9939	8.0188	7.8842	7.6582
		3	8.3359	8.0175	8.0470	7.9085	7.6836
		4	10.0275	9.5691	9.5282	9.4089	9.1273
		5	10.7927	10.3354	10.3217	10.1870	9.8692
		6	10.8539	10.4086	10.4107	10.2637	9.9486
	0.4	1	7.3730	6.9686	6.8879	6.8444	6.6064
		2	10.3279	9.7406	9.6041	9.5620	9.2175
		3	10.3828	9.7977	9.6667	9.6195	9.2755
		4	12.4489	11.7059	11.5011	11.4751	11.0541
		5	13.4721	12.6763	12.4656	12.4375	11.9714
		6	13.6051	12.8140	12.6154	12.5764	12.1103
	0.6	1	8.7206	8.1810	8.0225	8.0196	7.7132
		2	12.2184	11.4478	11.2095	11.2178	10.7806
		3	12.3022	11.5308	11.2960	11.3006	10.8623
		4	14.7299	13.7806	13.4684	13.4936	12.9626
		5	15.9572	14.9308	14.5973	14.6255	14.0430
		6	16.1536	15.1240	14.7975	14.8180	14.2322

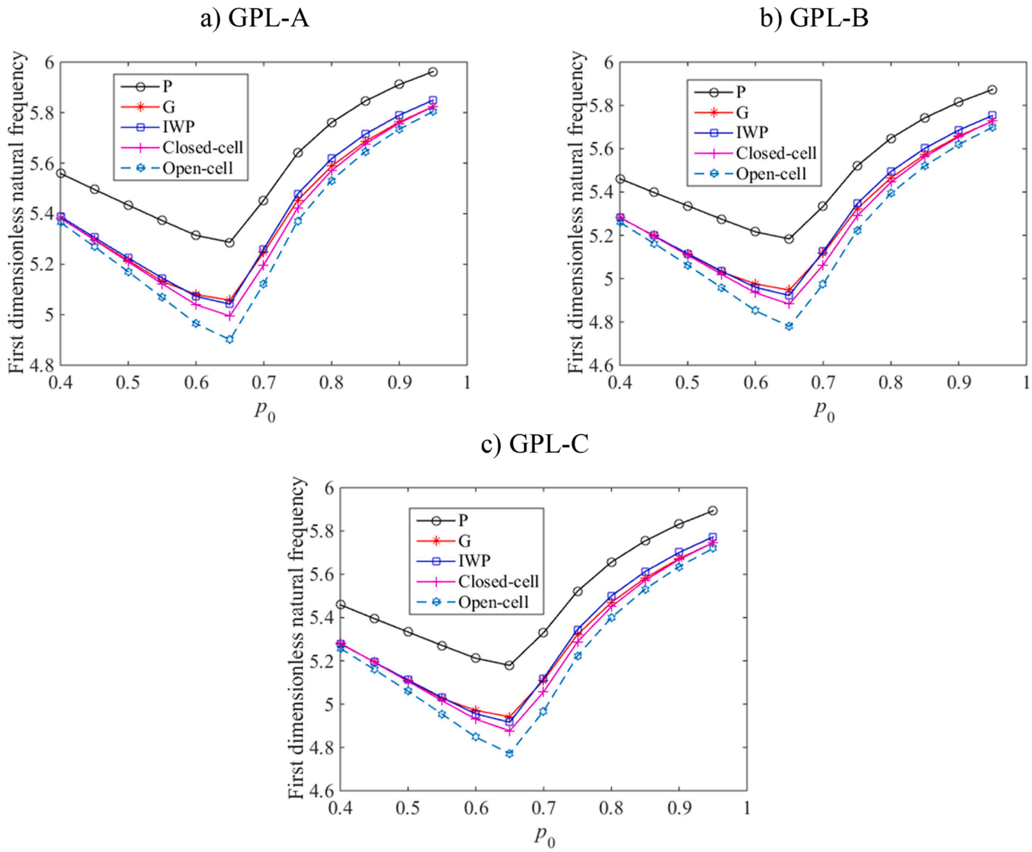

Fig. 3. The effect of porosity coefficient p_0 on the first frequency of the SSSS GPR-FG-TPMS microplate (P-II case, $a = 20h$, $l_0/h = 0.3$, $W_{GPL} = 0.01$).

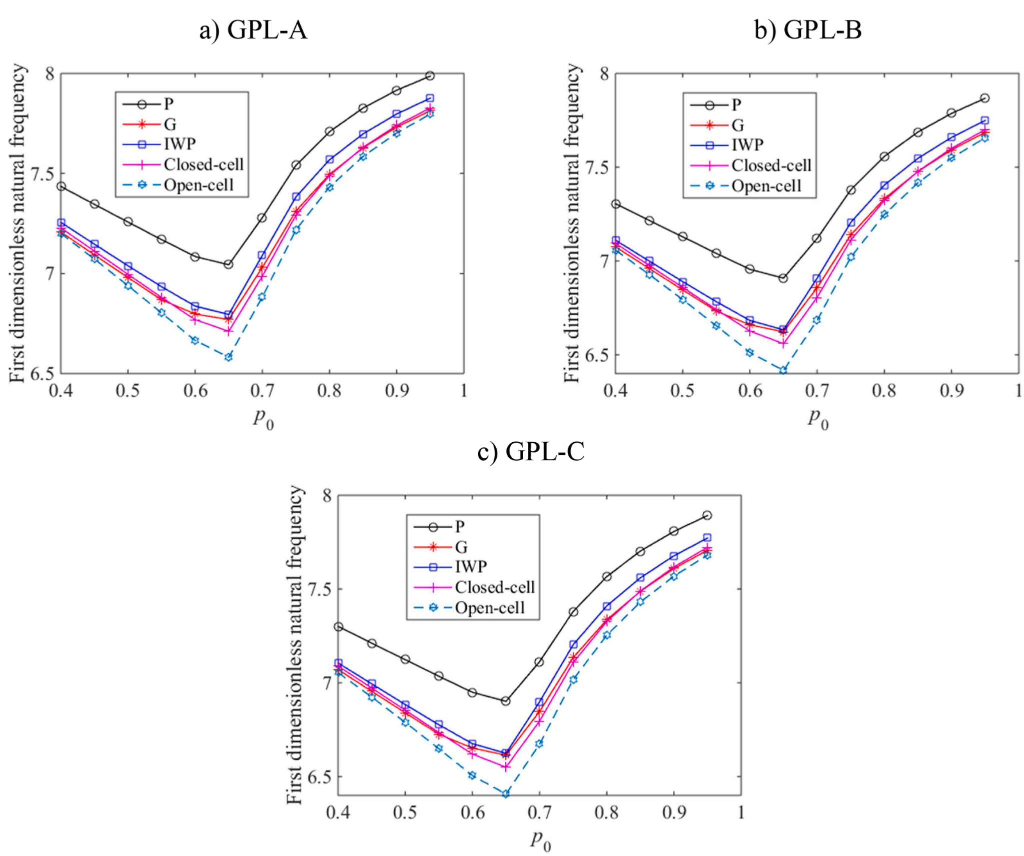

Fig. 4. The effect of porosity coefficient $p_0$on the first frequency of the CCCC GPR-FG-TPMS microplate (P-II case, $a = 20h$, $l_0/h = 0.3$, $W_{GPL} = 0.01$).

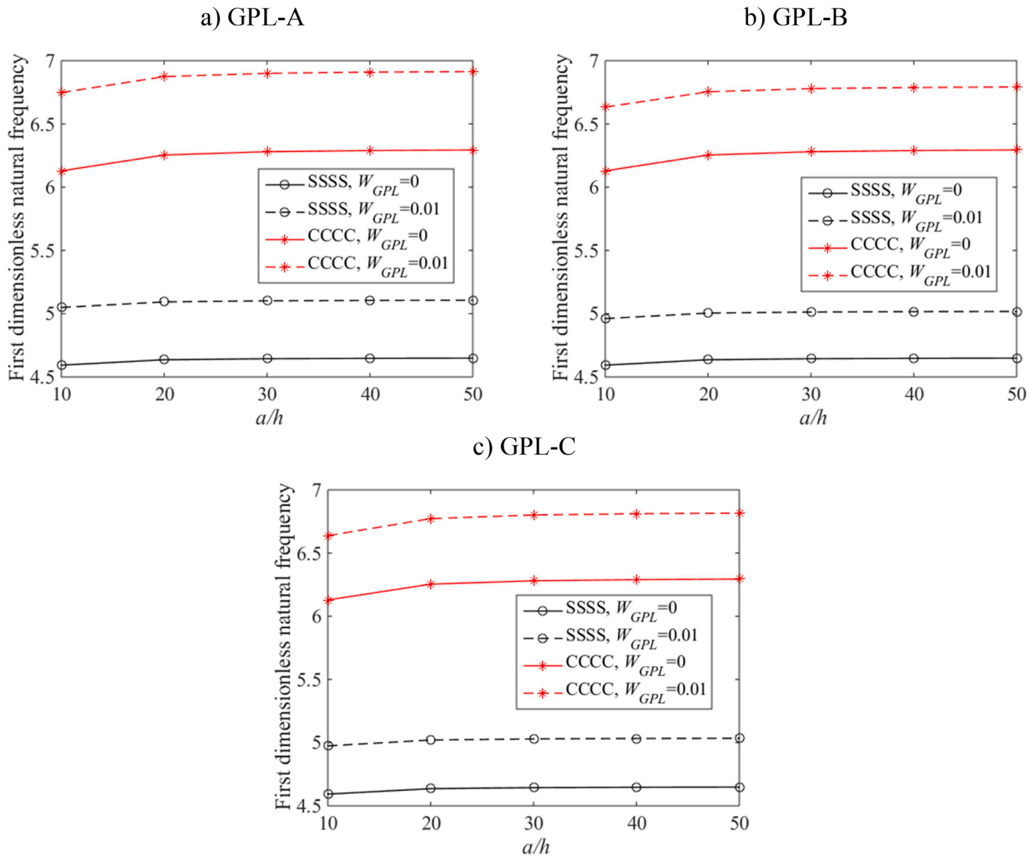

Fig. 5. The effect of length-to-thickness ratio on the first frequency of the Gyroid FG-TPMS and GPR-FG-TPMS microplate (P-I case, $l_0/h = 0.3$, $p_0 = 0.8$).

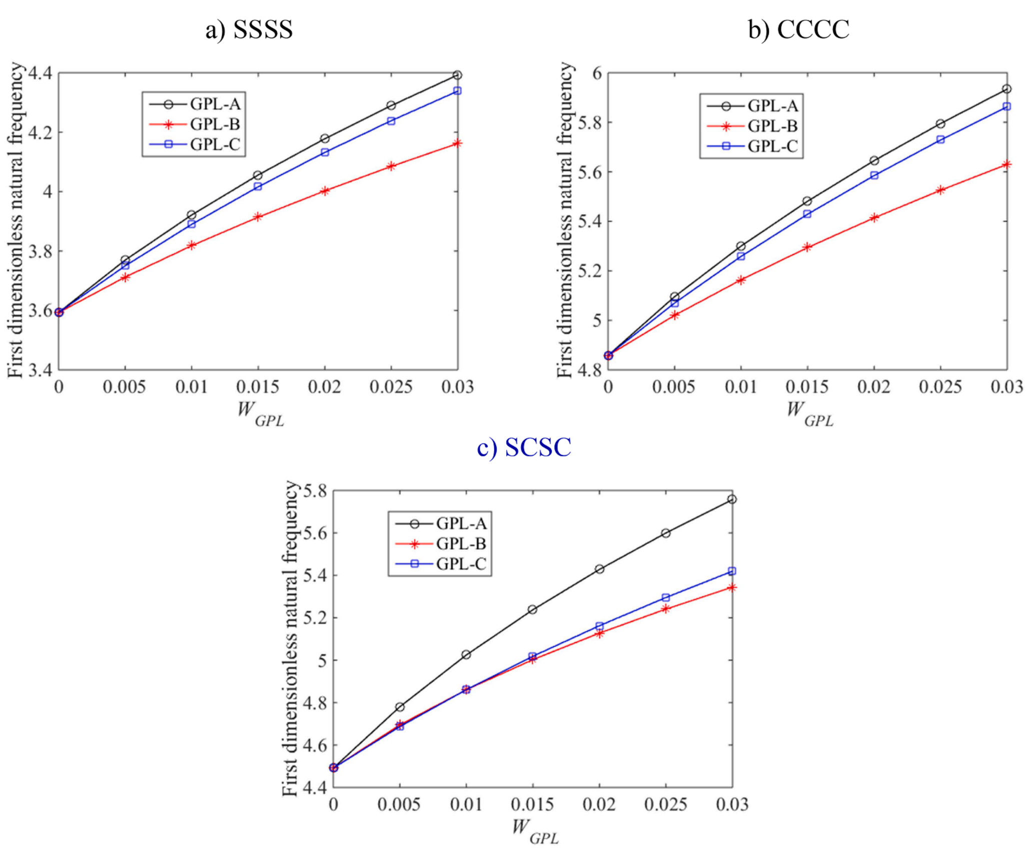

Fig. 6. The effect of W_{GPL} on the first frequency of the IWP GPR-FG-TPMS microplate (P-I case, $a/h = 20$, $l_0/h = 0.1$, $p_0 = 0.9$).

Table 7
The normalized central deflection of the SSSS GPR-FG-TPMS microplate ($a = 10h$, $p_0 = 0.7$, $W_{GPL} = 0.01$).

BCs	Porosity distribution	l_0/h	TPMS				
			P	G	IWP	Closed-cell	Open-Cell
SSSS	P-I	0.0	1.7491	1.8825	1.7362	1.9949	2.1257
		0.3	0.6670	0.7880	0.7877	0.8366	0.9283
		0.6	0.2336	0.2878	0.3000	0.3061	0.3474
		0.9	0.1121	0.1399	0.1478	0.1489	0.1702
	P-II	0.0	1.3686	1.5022	1.4081	1.5356	1.5633
		0.3	0.6054	0.7166	0.7153	0.7478	0.8044
		0.6	0.2269	0.2809	0.2921	0.2974	0.3337
		0.9	0.1111	0.1396	0.1473	0.1486	0.1694
	P-III	0.0	2.1573	2.3635	2.2111	2.5115	2.6584
		0.3	0.7678	0.9516	0.9896	1.0275	1.1634
		0.6	0.2630	0.3418	0.3730	0.3716	0.4338
		0.9	0.1256	0.1654	0.1831	0.1802	0.2122
CCCC	P-I	0.0	0.6631	0.6796	0.6079	0.7051	0.7641
		0.3	0.2255	0.2612	0.2573	0.2741	0.3049
		0.6	0.0758	0.0923	0.0956	0.0976	0.1105
		0.9	0.0360	0.0445	0.0468	0.0471	0.0537
	P-II	0.0	0.5083	0.5535	0.5085	0.5602	0.5874
		0.3	0.2035	0.2385	0.2352	0.2465	0.2667
		0.6	0.0730	0.0894	0.0925	0.0941	0.1053
		0.9	0.0353	0.0439	0.0462	0.0465	0.0527
	P-III	0.0	0.8113	0.8333	0.7405	0.8564	0.9159
		0.3	0.2635	0.3226	0.3301	0.3444	0.3924
		0.6	0.0884	0.1146	0.1245	0.1241	0.1453
		0.9	0.0421	0.0553	0.0611	0.0602	0.0710

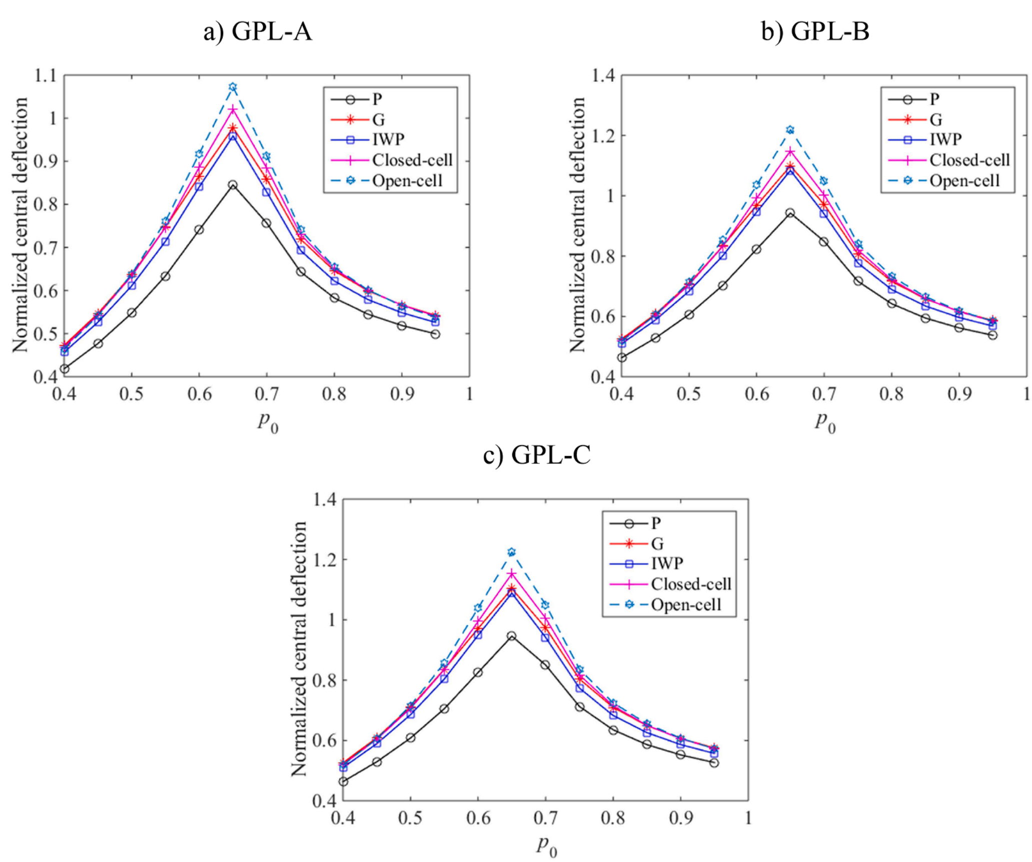

Fig. 7. The influence of porosity coefficient p_0 on the normalized central deflection of the SSSS GPR-FG-TPMS microplate (P-II case, $a = 20h$, $l_0/h = 0.2$, $W_{GPL} = 0.01$).

Additionally, the virtual kinetic energy of the microplate can be given

$$\delta T = \int_{\Omega} \delta \overline{\mathbf{u}}^T \mathbf{I}_m \ddot{\overline{\mathbf{u}}} \mathrm{d}\Omega \tag{30}$$

in which

$$\overline{\mathbf{u}} = \{ \mathbf{u}_1 \quad \mathbf{u}_2 \quad \mathbf{u}_3 \}^T;\ \mathbf{I}_m = \begin{bmatrix} \mathbf{I}_0 & 0 & 0 \\ 0 & \mathbf{I}_0 & 0 \\ 0 & 0 & \mathbf{I}_0 \end{bmatrix};\ \mathbf{I}_0 = \begin{bmatrix} I_1 & I_2 & I_4 \\ I_2 & I_3 & I_5 \\ I_4 & I_5 & I_6 \end{bmatrix} \tag{31}$$

where

$$(I_1, I_2, I_3, I_4, I_5, I_6) = \int_{-h/2}^{h/2} \rho(z)\left(1, z, z^2, f(z), zf(z), f^2(z)\right) \mathrm{d}z \tag{32}$$

The virtual work δW is defined by

$$\delta W = \int_{\Omega} f_0 \delta(w_b + w_s) \mathrm{d}\Omega \tag{33}$$

where f_0 denotes external transverse loads.

By inserting Eqs. (29), (30) and (33) into Eq. (27), we obtain

$$\begin{aligned} &\int_{\Omega} \delta(\overline{\boldsymbol{\varepsilon}}_b) \overline{\mathbf{C}}_u \overline{\boldsymbol{\varepsilon}}_b \mathrm{d}\Omega + \int_{\Omega} \delta(\boldsymbol{\gamma}_s)^T \overline{\mathbf{C}}_s \boldsymbol{\gamma}_s \mathrm{d}\Omega + \int_{\Omega} \delta(\overline{\boldsymbol{\chi}}_b)^T \overline{\mathbf{C}}_{rb} \Gamma_{rb} \overline{\boldsymbol{\chi}}_b \mathrm{d}\Omega \\ &+ \int_{\Omega} \delta(\overline{\boldsymbol{\chi}}_s)^T \overline{\mathbf{C}}_{rs} \Gamma_{rs} \overline{\boldsymbol{\chi}}_s \mathrm{d}\Omega + \int_{\Omega} \delta \overline{\boldsymbol{\xi}}^T \overline{\mathbf{C}}_{dil} \overline{\boldsymbol{\xi}} \mathrm{d}\Omega + \int_{\Omega} \delta(\overline{\boldsymbol{\eta}}_b)^T \overline{\mathbf{C}}_{deb} \Gamma_{deb} \overline{\boldsymbol{\eta}}_b \mathrm{d}\Omega \\ &+ \int_{\Omega} \delta(\overline{\boldsymbol{\eta}}_s)^T \overline{\mathbf{C}}_{des} \Gamma_{des} \overline{\boldsymbol{\eta}}_s \mathrm{d}\Omega + \int_{\Omega} \delta \overline{\mathbf{u}}^T \mathbf{I}_m \ddot{\overline{\mathbf{u}}} \mathrm{d}\Omega = \int_{\Omega} f_0 \delta(w_b + w_s) \mathrm{d}\Omega \end{aligned} \tag{34}$$

$$\begin{aligned} \mathbf{K} = &\int_{\Omega} (\overline{\mathbf{B}}_b)^T \overline{\mathbf{C}}_u \overline{\mathbf{B}}_b \mathrm{d}\Omega + \int_{\Omega} (\overline{\mathbf{B}}_s)^T \overline{\mathbf{C}}_s \overline{\mathbf{B}}_s \mathrm{d}\Omega + \int_{\Omega} (\overline{\mathbf{B}}_{rb})^T \overline{\mathbf{C}}_{rb} \Gamma_{rb} \overline{\mathbf{B}}_{rb} \mathrm{d}\Omega + \int_{\Omega} (\overline{\mathbf{B}}_{rs})^T \overline{\mathbf{C}}_{rs} \Gamma_{rs} \overline{\mathbf{B}}_{rs} \mathrm{d}\Omega \\ &+ \int_{\Omega} \left(\overline{\mathbf{B}}^{dil}\right)^T \overline{\mathbf{C}}_{dil} \overline{\mathbf{B}}^{dil} \mathrm{d}\Omega + \int_{\Omega} \left(\overline{\mathbf{B}}^{deb}\right)^T \overline{\mathbf{C}}_{deb} \Gamma_{deb} \overline{\mathbf{B}}^{deb} \mathrm{d}\Omega + \int_{\Omega} \left(\overline{\mathbf{B}}^{des}\right)^T \overline{\mathbf{C}}_{des} \Gamma_{des} \overline{\mathbf{B}}^{des} \mathrm{d}\Omega \\ \mathbf{M} = &\int_{\Omega} \overline{\mathbf{N}}^T \mathbf{I}_m \overline{\mathbf{N}} \mathrm{d}\Omega;\ \mathbf{d} = \widetilde{\mathbf{d}} e^{i\omega t};\ \mathbf{F} = \int_{\Omega} f_0 \{ 0 \quad 0 \quad N_i \quad N_i \}^T \mathrm{d}\Omega \end{aligned} \tag{42}$$

2.4. Isogeometric approximation

The displacement of the microplate is expressed as an approximation using the NURBS function [55], and is presented as follows

$$\mathbf{u}^h(\varsigma, \xi) = \sum_{i=1}^{m \times n} \mathbf{N}_i(\varsigma, \xi) \mathbf{d}_i \tag{35}$$

in which

$$\mathbf{N}_i(\varsigma, \xi) = \begin{bmatrix} N_i(\varsigma,\xi) & 0 & 0 & 0 \\ 0 & N_i(\varsigma,\xi) & 0 & 0 \\ 0 & 0 & N_i(\varsigma,\xi) & 0 \\ 0 & 0 & 0 & N_i(\varsigma,\xi) \end{bmatrix};\ \mathbf{d}_i = \begin{Bmatrix} u_i \\ v_i \\ w_{bi} \\ w_{si} \end{Bmatrix} \tag{36}$$

where $N_i(\varsigma,\xi)$ and $\mathbf{d}_i$ correspond in the NURBS basis function and nodal degrees of freedom vector for the i^{th} control point, respectively and m and n are the number of control points in the x and y directions.

According to the approximation in Eq. (35), the bending and shear strain tensors in Eq. (15) are rewritten as follows:

$$\overline{\varepsilon}_b = \sum_{i=1}^{m \times n} \{ \mathbf{B}_{b1i} \quad \mathbf{B}_{b2i} \quad \mathbf{B}_{b3i} \}^T \mathbf{d}_i = \sum_{i=1}^{m \times n} \overline{\mathbf{B}}_{bi} \mathbf{d}_i;\ \gamma_s = \sum_{i=1}^{m \times n} \overline{\mathbf{B}}_{si} \mathbf{d}_i \tag{37}$$

The higher-order strain tensors based on Eq. (35) can be reformed as follows

$$\begin{aligned} \overline{\chi}_b &= \{ \chi_{b1} \quad \chi_{b2} \}^T = \sum_{i=1}^{m \times n} \{ \mathbf{B}_{rb1i} \quad \mathbf{B}_{rb2i} \}^T \mathbf{d}_i = \sum_{i=1}^{m \times n} \overline{\mathbf{B}}_{rbi} \mathbf{d}_i \\ \overline{\chi}_s &= \{ \chi_{s1} \quad \chi_{s2} \}^T = \sum_{i=1}^{m \times n} \{ \mathbf{B}_{rs1i} \quad \mathbf{B}_{rs2i} \}^T \mathbf{d}_i = \sum_{i=1}^{m \times n} \overline{\mathbf{B}}_{rsi} \mathbf{d}_i \\ \overline{\xi} &= \{ \xi_1 \quad \xi_2 \quad \xi_3 \quad \xi_4 \}^T = \sum_{i=1}^{m \times n} \{ \mathbf{B}_{1i}^{dil} \quad \mathbf{B}_{2i}^{dil} \quad \mathbf{B}_{3i}^{dil} \quad \mathbf{B}_{4i}^{dil} \}^T \mathbf{d}_i = \sum_{i=1}^{m \times n} \overline{\mathbf{B}}_i^{dil} \mathbf{d}_i \\ \overline{\eta}_b &= \{ \eta_{b1} \quad \eta_{b2} \quad \eta_{b3} \quad \eta_{b4} \}^T = \sum_{i=1}^{m \times n} \{ \mathbf{B}_{1i}^{deb} \quad \mathbf{B}_{2i}^{deb} \quad \mathbf{B}_{3i}^{deb} \quad \mathbf{B}_{4i}^{deb} \}^T \mathbf{d}_i = \sum_{i=1}^{m \times n} \overline{\mathbf{B}}_i^{deb} \mathbf{d}_i \\ \overline{\eta}_s &= \{ \eta_{s1} \quad \eta_{s2} \}^T = \sum_{i=1}^{m \times n} \{ \mathbf{B}_{1i}^{des} \quad \mathbf{B}_{2i}^{des} \}^T \mathbf{d}_i = \sum_{i=1}^{m \times n} \mathbf{B}_i^{des} \mathbf{d}_i \end{aligned} \tag{38}$$

Besides, the displacement vector $\overline{\mathbf{u}}$ is re-expressed as follows

$$\overline{\mathbf{u}} = \{ \mathbf{u}_1 \quad \mathbf{u}_2 \quad \mathbf{u}_3 \}^T = \sum_{i=1}^{m \times n} \{ \mathbf{N}_{1i} \quad \mathbf{N}_{2i} \quad \mathbf{N}_{3i} \}^T \mathbf{d}_i = \sum_{i=1}^{m \times n} \overline{\mathbf{N}}_i \mathbf{d}_i \tag{39}$$

The variational formulation for the free vibration and static bending of the GPR-FG-TPMS microplate is derived by substituting Eqs. (38) and (39) into Eq. (34) as follows

$$\left(\mathbf{K} - \omega^2 \mathbf{M}\right) \widetilde{\mathbf{d}} = 0 \tag{40}$$

$$\mathbf{K}\mathbf{d} = \mathbf{F} \tag{41}$$

where

where **K, M, F**, ω and $\widetilde{\mathbf{d}}$ denote global stiffness matrix, mass matrix, force vector, natural frequency, and mode shapes, respectively.

3. Numerical results

We now consider a FG-TPMS microplate with the material properties listed in Table 2. To study the size dependence, it is assumed that all three LSPs are identical ($l_1 = l_2 = l_3 = l_0$) [54]. Besides, the numerical results focus on the non-dimensional natural frequencies and central deflections, as outlined below:

$$\varpi = \sqrt{\omega L^2 \sqrt{\frac{\rho_s h}{D_s}}};\ \overline{w} = \frac{100 D_s \widehat{w}\left(\frac{a}{2}, \frac{b}{2}, 0\right)}{f_0 a^4} \quad \text{where } D_s = \frac{E_s h^3}{12\left(1 - \nu_s^2\right)} \tag{43}$$

3.1. Verification

To evaluate the accuracy of the proposed model, this study analyzes FG-TPMS plates according to the model described in reference [39]. The scale effect is ignored in this case ($l_0 = 0$). Bending and free vibration of the FG-TPMS plate are investigated under varying TPMS unit cells, density porosity distributions and density porosity coefficients (p_0). The boundary conditions are characterized by simply supported (S) and clamped (C) edge constraints. For instance, the SCSC plate configuration

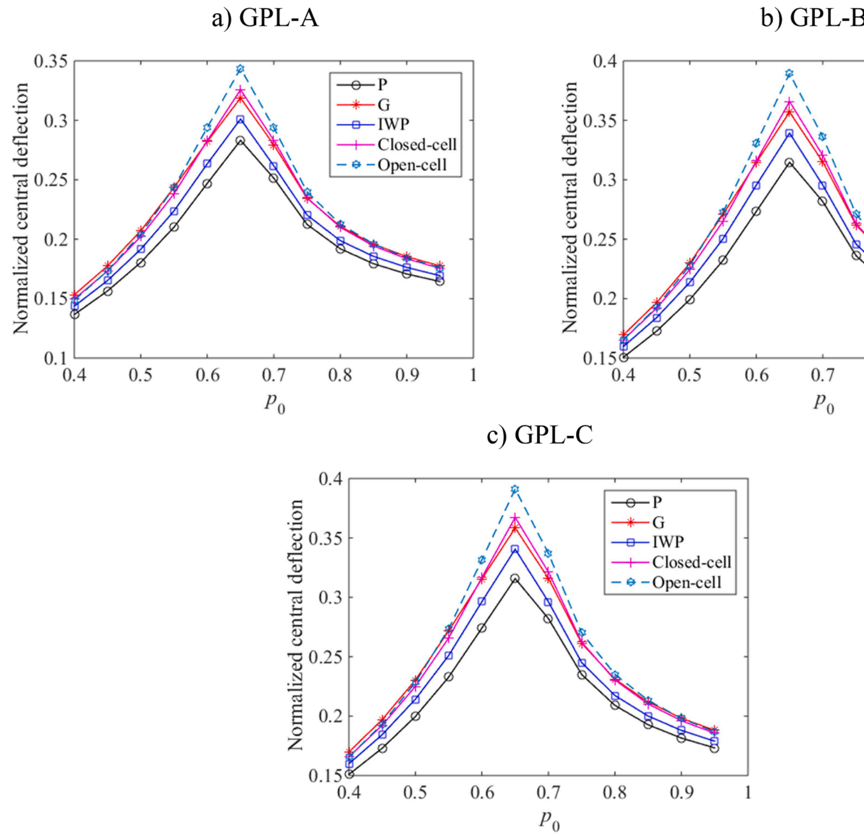

Fig. 8. The influence of porosity coefficient p_0 on the normalized central deflection $\overline{w}$ of the CCCC GPR-FG-TPMS microplate (P-II case, $a = 20h$, $l_0/h = 0.2$, $W_{GPL} = 0.01$).

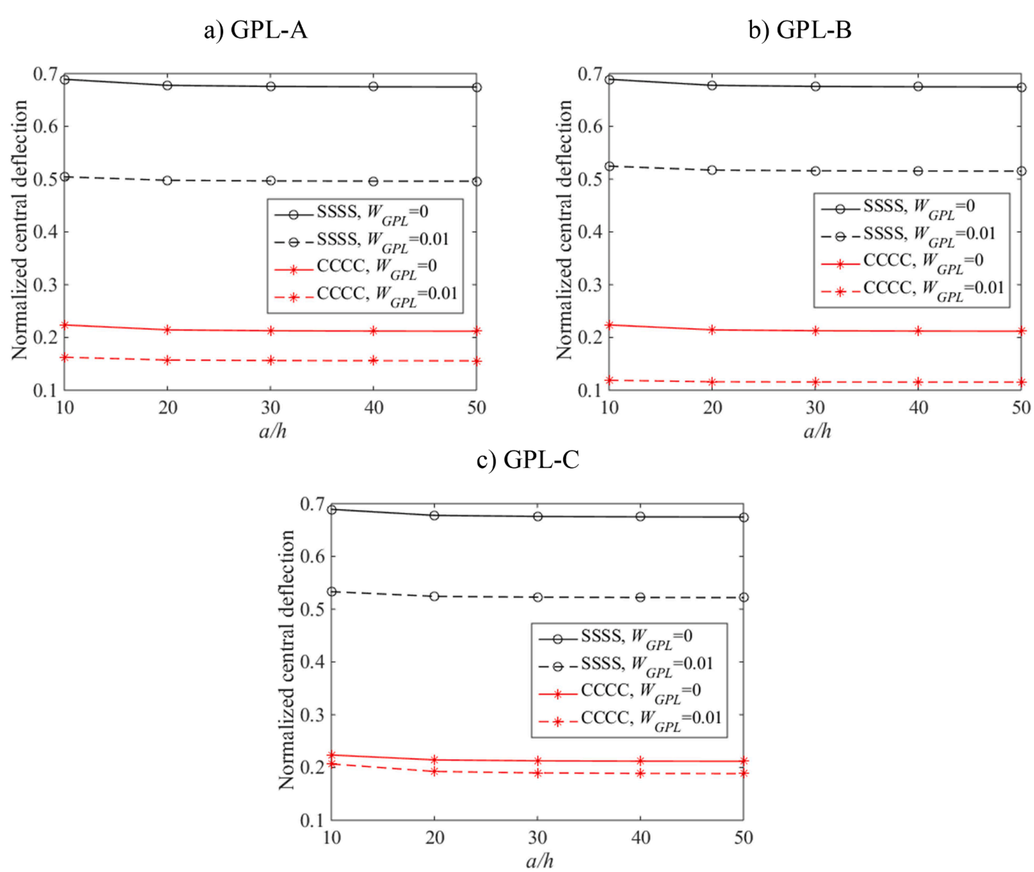

Fig. 9. The influence of length-to-thickness ratio on the normalized central deflection of SSSS Gyroid FG-TPMS and GPR-FG-TPMS microplates (P-I case, $l_0/h = 0.4$, $p_0 = 0.8$).

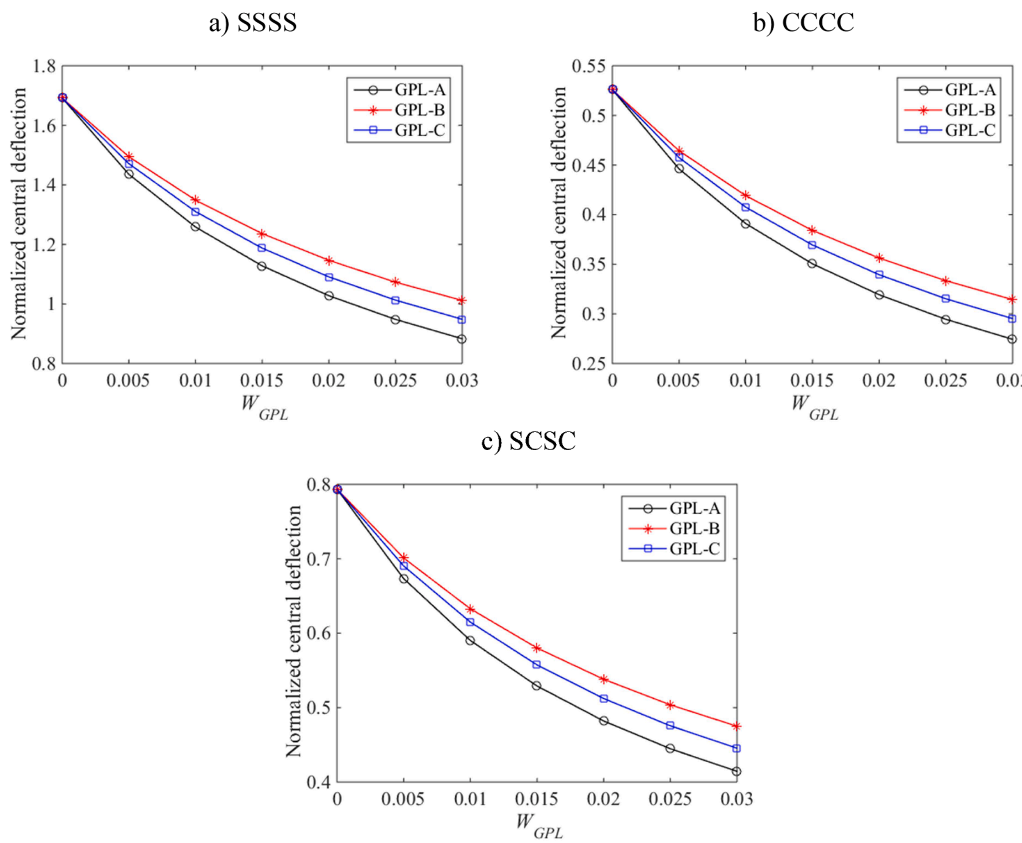

Fig. 10. The effect of W_{GPL} on the normalized central deflection of the IWP GPR-FG-TPMS square microplate (P-I case, $a/h = 20$, $l_0/h = 0.2$, $p_0 = 0.9$).

denotes a plate structure with two simply supported edges and two clamped edges. The investigation examines natural frequency and deflection characteristics of FG-TPMS plates through comprehensive parametric studies involving three TPMS distributions, two cellular solid configurations, density distribution patterns, varying thickness ratios (a/h) and porosity parameters (p_0). Tables 3 and 4 show the first frequency ($\overline{\varpi}$) and central deflection ($\overline{w}$) of a SSSS FG-TPMS square plate, respectively. The obtained results are compared with those from ref [39]. using a generalized HSDT with five variables and IGA. The close match between the two data sets validates the accuracy of the proposed method, confirming its suitability for such analyses.

3.2. Free vibration behaviors

This subsection presents innovative computational insights into the free vibration analysis. Tables 5 and 6 outline the effect of LSPs, density distribution patterns and TPMS unit cells on the lowest six dimensionless natural frequencies of the SSSS and CCCC GPR-FG-TPMS square microplates, respectively. An increase in l_0/h leads to higher natural frequencies, because of the stronger influence of non-classical effects and the resulting stiffness enhancement. In the absence of size effects ($l_0/h = 0$), the IWP GPR-FG-TPMS plate achieves the highest frequencies for P-I and P-III distributions, while the Primitive configuration performs best under the P-II distribution. When size effects are accounted for ($l_0/h \neq 0$), the Primitive GPR-FG-TPMS microplate exhibits superior vibrational stiffness across all distribution types. Among the density porosity distributions, the microplate with a P-II distribution demonstrates the maximum frequency, while the minimum frequency is observed in the P-III distribution. Figs. 3 and 4 present effects of p_0 on the vibrational behavior of the SSSS and CCCC GPRC-FG-TPMS microplate, respectively. The data in Figs. 3 and 4 demonstrate that the natural frequency of the GPRC-FG-TPMS microplate increases when the density porosity coefficient increases for the case $p_0 > 0.65$. Conversely, when $p_0 < 0.65$, the trend follows the opposite pattern. Next, the first frequency of the FG-TPMS ($W_{GPL} = 0$) and GPR-FG-TPMS ($W_{GPL} = 0.01$) microplates is performed and shown in Fig. 5. It can be seen that increasing the length-to-thickness ratio leads to a higher vibrational frequency. Besides, a distinct difference is observed between the FG-TPMS and GPR-FG-TPMS microplates. The performance improvement is primarily attributed to the exceptional mechanical properties and high stiffness-to-weight ratio of GPLs, which enhance the vibrational stiffness of the microplate without causing a significant increase in mass. This comparison further highlights the advantages of employing GPR-FG-TPMS microplates over conventional FG-TPMS designs, especially in applications requiring lightweight structures with superior high-frequency performance. The incorporation of GPLs significantly enhances the natural frequency. Fig. 6 shows the variation of the first dimensionless natural frequency of the IWP GPR-FG-TPMS microplate. We can see that when the GPLs weight fraction grows, the vibrational stiffness of the microplate rises for all distribution types due to the stiffening effect provided by the GPLs. Besides, the GPR-FG-TPMS microplate with GPL-A distribution exhibits the highest natural frequency, while the GPL-B distribution shows the lowest frequency. This indicates that allocating more GPLs near the top and bottom surfaces (as in GPL-A) significantly enhances the vibrational stiffness of the microplate. In contrast, the GPL-B pattern, which concentrates reinforcements near the mid-plane, contributes less effectively to the dynamic stiffness improvement. These observations confirm the crucial role of GPL distribution patterns in governing the vibrational behavior of GPR-FG-TPMS microplates and provide valuable insights for the optimal design of vibration-sensitive microscale structures.

3.3. Bending analysis

New computational insights into bending analysis of a GPR-FG-TPMS microplate are introduced in this subsection. The effect of LSPs on the normalized central deflection of the GPR-FG-TPMS microplate is outlined in Table 7. We can see that the bending stiffness is enriched with a rise in the scale-to-thickness ratio. In addition, with the size effect neglected, the Primitive GPR-FG-TPMS plates attain the most minor deflection for the P-II distribution, while the IWP GPR-FG-TPMS plate achieves the minimal deflection for the P-I and P-III distributions. Besides, the GPR-FG-TPMS microplate with Primitive unit cells achieves the slightest deflection, surpassing those with other unit cells. Figs. 7 and 8 illustrate how the density porosity coefficient affects the central deflection of the SSSS and CCCC GPRC-FG-TPMS microplate, respectively. According to the data, when the density porosity coefficient exceeds 0.65, the dimensionless central deflection of the GPRC-FG-TPMS microplate decreases. In contrast, for p_0 values below 0.65, the trend is reversed. Next, the impact of the length-to-thickness ratio on the static bending of the Gyroid FG-TPMS (W_{GPL}=0) and GPR-FG-TPMS (W_{GPL}=0.01) microplates is investigated and presented in Fig. 9. The numerical results in Fig. 9 show that the central deflection of the GPR-FG-TPMS microplates is smaller than the central deflection of the FG-TPMS microplate. The reason is that the incorporation of GPLs significantly improves the flexural rigidity of the microplate. Finally, Fig. 10 shows how the GPLs distribution and GPL's weight fraction influence the normalized central deflection of the IWP GPR-FG-TPMS microplate. It can be seen in Fig. 10, increasing the GPLs weight fraction leads to a decreased central deflection of the GPR-FG-TPMS microplates due to the stiffening effect of GPLs. The GPL-A pattern consistently exhibits the lowest central deflection values among the GPL distributions, indicating superior reinforcement efficiency. Conversely, the GPL-B pattern shows the highest deflection values, while the GPL-C distribution provides intermediate performance.

4. Conclusions

Small scale effects in the GPR-FG-TPMS microplate were investigated considering three types of TPMS (Primitive, Gyroid and IWP) and two cellular configurations (closed-cell and open-cell). The analysis employed a coupled framework integrated both RPT, MGST and IGA. This research examined the influence of LSPs, unit cell types, density and GPLS distributions, and geometrical configurations on the natural frequencies and deflections of the GPR-FG-TPMS microplate. The numerical results reveal the following insights:

- The natural frequencies are increased and deflections are decreased when increasing the length-scale parameters.
- When the size effect is ignored, the Primitive GPR-FG-TPMS plates show the highest vibrational and bending stiffness for the P-II distribution, whereas the IWP GPR-FG-TPMS plates demonstrate the highest stiffness under P-I and P-III distributions.
- At the micro-scale level, the GPR-FG-TPMS microplate with Primitive unit cells outperforms other unit cell types by achieving vibrational and bending stiffness.
- The highest bending and vibrational stiffness are observed in GPR-FG-TPMS microplate with a GPL-A distribution, while the GPL-B distribution results in the lowest stiffness.
- The GPR-FG-TPMS microplate with a P-II density distribution provides the highest natural frequencies and the smallest deflections, while the microplate with a P-III density distribution exhibits the lowest natural frequencies and the largest deflections.
- An increase in the length-to-thickness ratio enhances the stiffness of the GPR-FG-TPMS microplate.

CRediT authorship contribution statement

P.T. Hung: Writing – review & editing, Visualization, Methodology, Conceptualization, Funding acquisition. **M. Abdel-Wahab:** Writing – review & editing, Visualization, Validation. **P. Phung-Van:** Writing – original draft, Visualization, Validation, Investigation, Conceptualization. **Chien H. Thai:** Writing – review & editing, Visualization, Methodology, Conceptualization.

Declaration of competing interest

The authors state that there is no potential conflict of interest and no ethical statement in this paper.

Acknowledgements

This research is funded by Vietnam National Foundation for Science and Technology Development (NAFOSTED) under grant number 107.02–2023.79.

Appendix

$$\boldsymbol{\varepsilon}_b = \begin{Bmatrix} \varepsilon_x \\ \varepsilon_y \\ \gamma_{xy} \end{Bmatrix}; \boldsymbol{\varepsilon}_s = \begin{Bmatrix} \gamma_{xz} \\ \gamma_{yz} \end{Bmatrix}; \boldsymbol{\varepsilon}_{b1} = \begin{Bmatrix} u_{,x} \\ v_{,y} \\ u_{,y} + v_{,x} \end{Bmatrix}; \boldsymbol{\varepsilon}_{b2} = -\begin{Bmatrix} w_{b,xx} \\ w_{b,yy} \\ 2w_{b,xy} \end{Bmatrix}; \boldsymbol{\varepsilon}_{b3} = \begin{Bmatrix} w_{s,xx} \\ w_{s,yy} \\ 2w_{s,xy} \end{Bmatrix}; \gamma_s = \begin{Bmatrix} w_{s,x} \\ w_{s,y} \end{Bmatrix} \tag{A1}$$

$$\chi_{b1} = \frac{1}{4}\begin{Bmatrix} 4w_{b,xy} + 2w_{s,xy} \\ -4w_{b,xy} - 2w_{s,xy} \\ 2\left(w_{b,yy} - w_{b,xx}\right) + \left(w_{s,yy} - w_{s,xx}\right) \end{Bmatrix}; \ \chi_{b2} = \frac{1}{4}\begin{Bmatrix} -2w_{s,xy} \\ 2w_{s,xy} \\ w_{s,xx} - w_{s,yy} \end{Bmatrix}$$
$$\chi_{s1} = \frac{1}{4}\begin{Bmatrix} v_{,xx} - u_{,xy} \\ v_{,xy} - u_{,yy} \end{Bmatrix}; \ \chi_{s2} = \frac{1}{4}\begin{Bmatrix} -w_{s,y} \\ w_{s,x} \end{Bmatrix}; f''(z) = \frac{\mathrm{d}^2 f(z)}{\mathrm{d}z^2} \tag{A2}$$

$$\boldsymbol{\xi}_1 = \begin{Bmatrix} u_{,xx} + v_{,xy} \\ v_{,yy} + u_{,xy} \\ -w_{b,xx} - w_{b,yy} \end{Bmatrix};\ \boldsymbol{\xi}_2 = -\begin{Bmatrix} w_{b,xxx} + w_{b,xyy} \\ w_{b,yyy} + w_{b,xxy} \\ 0 \end{Bmatrix};\ \boldsymbol{\xi}_3 = \begin{Bmatrix} w_{s,xxx} + w_{s,xyy} \\ w_{s,yyy} + w_{s,xxy} \\ 0 \end{Bmatrix};\ \boldsymbol{\xi}_4 = \begin{Bmatrix} 0 \\ 0 \\ w_{s,xx} + w_{s,yy} \end{Bmatrix} \tag{A3}$$

$$\boldsymbol{\eta}_{b1} = \begin{Bmatrix} \frac{2}{5}u_{,xx} - \frac{1}{5}u_{,yy} - \frac{2}{5}v_{,xy} \\ \frac{2}{5}v_{,yy} - \frac{1}{5}v_{,xx} - \frac{2}{5}u_{,xy} \\ -\frac{1}{5}u_{,xx} + \frac{4}{15}u_{,yy} + \frac{8}{15}v_{,xy} \\ -\frac{1}{5}v_{,yy} + \frac{4}{15}v_{,xx} + \frac{8}{15}u_{,xy} \\ -\frac{1}{5}u_{,xx} - \frac{1}{15}u_{,yy} - \frac{2}{15}v_{,xy} \\ -\frac{1}{5}v_{,yy} - \frac{1}{15}v_{,xx} - \frac{2}{15}u_{,xy} \end{Bmatrix};\ \boldsymbol{\eta}_{b2} = \begin{Bmatrix} -\frac{2}{5}w_{b,xxx} + \frac{3}{5}w_{b,xyy} \\ -\frac{2}{5}w_{b,yyy} + \frac{3}{5}w_{b,xxy} \\ \frac{1}{5}w_{b,xxx} - \frac{4}{5}w_{b,xyy} \\ \frac{1}{5}w_{b,yyy} - \frac{4}{5}w_{b,xxy} \\ \frac{1}{5}w_{b,xxx} + \frac{1}{5}w_{b,xyy} \\ \frac{1}{5}w_{b,yyy} + \frac{1}{5}w_{b,xxy} \end{Bmatrix};\ \boldsymbol{\eta}_{b3} = \begin{Bmatrix} \frac{2}{5}w_{s,xxx} - \frac{3}{5}w_{s,xyy} \\ \frac{2}{5}w_{s,yyy} - \frac{3}{5}w_{s,xxy} \\ -\frac{1}{5}w_{s,xxx} + \frac{4}{5}w_{s,xyy} \\ -\frac{1}{5}w_{s,yyy} + \frac{4}{5}w_{s,xxy} \\ -\frac{1}{5}w_{s,xxx} - \frac{1}{5}w_{s,xyy} \\ -\frac{1}{5}w_{s,yyy} - \frac{1}{5}w_{s,xxy} \end{Bmatrix}$$

$$\boldsymbol{\eta}_{b4} = \begin{Bmatrix} -\frac{1}{5}w_{s,x} \\ -\frac{1}{5}w_{s,y} \\ -\frac{1}{15}w_{s,x} \\ -\frac{1}{15}w_{s,y} \\ \frac{4}{15}w_{s,x} \\ \frac{4}{15}w_{s,y} \end{Bmatrix};\ \boldsymbol{\eta}_{s1} = \begin{Bmatrix} \frac{1}{5}w_{b,xx} + \frac{1}{5}w_{b,yy} - \frac{1}{5}w_{s,xx} - \frac{1}{5}w_{s,yy} \\ -\frac{4}{15}w_{b,xx} + \frac{1}{15}w_{b,yy} + \frac{4}{15}w_{s,xx} - \frac{1}{15}w_{s,yy} \\ -\frac{4}{15}w_{b,yy} + \frac{1}{15}w_{b,xx} + \frac{4}{15}w_{s,yy} - \frac{1}{15}w_{s,xx} \\ -\frac{1}{3}w_{b,xy} + \frac{1}{3}w_{s,xy} \end{Bmatrix};\ \boldsymbol{\eta}_{s2} = \begin{Bmatrix} -\frac{2}{5}w_{s,xx} - \frac{2}{5}w_{s,yy} \\ \frac{8}{15}w_{s,xx} - \frac{2}{15}w_{s,yy} \\ \frac{8}{15}w_{s,yy} - \frac{2}{15}w_{s,xx} \\ \frac{2}{3}w_{s,xy} \end{Bmatrix} \tag{A4}$$

$$\begin{gathered} \overline{\boldsymbol{\varepsilon}}_b = \{\boldsymbol{\varepsilon}_{b1} \quad \boldsymbol{\varepsilon}_{b2} \quad \boldsymbol{\varepsilon}_{b3}\}^T;\ \overline{\boldsymbol{\chi}}_b = \{\boldsymbol{\chi}_{b1} \quad \boldsymbol{\chi}_{b2}\}^T;\ \overline{\boldsymbol{\chi}}_s = \{\boldsymbol{\chi}_{s1} \quad \boldsymbol{\chi}_{s2}\}^T \\ \overline{\boldsymbol{\xi}} = \{\boldsymbol{\xi}_1 \quad \boldsymbol{\xi}_2 \quad \boldsymbol{\xi}_3 \quad \boldsymbol{\xi}_4\}^T;\ \overline{\boldsymbol{\eta}}_b = \{\boldsymbol{\eta}_{b1} \quad \boldsymbol{\eta}_{b2} \quad \boldsymbol{\eta}_{b3} \quad \boldsymbol{\eta}_{b4}\}^T;\ \overline{\boldsymbol{\eta}}_s = \{\boldsymbol{\eta}_{s1} \quad \boldsymbol{\eta}_{s2}\}^T \\ \overline{\mathbf{C}}_u = \begin{bmatrix} \mathbf{A}_b & \mathbf{B}_b & \mathbf{E}_b \\ \mathbf{B}_b & \mathbf{D}_b & \mathbf{F}_b \\ \mathbf{E}_b & \mathbf{F}_b & \mathbf{H}_b \end{bmatrix};\ \overline{\mathbf{C}}_{dil} = \begin{bmatrix} \mathbf{A}_{dil} & \mathbf{B}_{dil} & \mathbf{C}_{dil} & \mathbf{E}_{dil} \\ \mathbf{B}_{dil} & \mathbf{D}_{dil} & \mathbf{F}_{dil} & \mathbf{L}_{dil} \\ \mathbf{C}_{dil} & \mathbf{F}_{dil} & \mathbf{H}_{dil} & \mathbf{O}_{dil} \\ \mathbf{E}_{dil} & \mathbf{L}_{dil} & \mathbf{O}_{dil} & \mathbf{P}_{dil} \end{bmatrix};\ \overline{\mathbf{C}}_{deb} = \begin{bmatrix} \mathbf{A}_{deb} & \mathbf{B}_{deb} & \mathbf{C}_{deb} & \mathbf{E}_{deb} \\ \mathbf{B}_{deb} & \mathbf{D}_{deb} & \mathbf{F}_{deb} & \mathbf{L}_{deb} \\ \mathbf{C}_{deb} & \mathbf{F}_{deb} & \mathbf{H}_{deb} & \mathbf{O}_{deb} \\ \mathbf{E}_{deb} & \mathbf{L}_{deb} & \mathbf{O}_{deb} & \mathbf{P}_{deb} \end{bmatrix} \\ \overline{\mathbf{C}}_{rb} = \begin{bmatrix} \mathbf{A}_{rb} & \mathbf{B}_{rb} \\ \mathbf{B}_{rb} & \mathbf{D}_{rb} \end{bmatrix};\ \overline{\mathbf{C}}_{rs} = \begin{bmatrix} \mathbf{A}_{rs} & \mathbf{B}_{rs} \\ \mathbf{B}_{rs} & \mathbf{D}_{rs} \end{bmatrix};\ \overline{\mathbf{C}}_{des} = \begin{bmatrix} \mathbf{A}_{des} & \mathbf{B}_{des} \\ \mathbf{B}_{des} & \mathbf{D}_{des} \end{bmatrix} \\ \overline{\Gamma}_{rb} = \begin{bmatrix} \boldsymbol{\Gamma}_{rb} & 0 \\ 0 & \boldsymbol{\Gamma}_{rb} \end{bmatrix};\ \overline{\Gamma}_{rs} = \begin{bmatrix} \boldsymbol{\Gamma}_{rs} & 0 \\ 0 & \boldsymbol{\Gamma}_{rs} \end{bmatrix};\ \overline{\Gamma}_{deb} = \begin{bmatrix} \boldsymbol{\Gamma}_{deb} & 0 & 0 & 0 \\ 0 & \boldsymbol{\Gamma}_{deb} & 0 & 0 \\ 0 & 0 & \boldsymbol{\Gamma}_{deb} & 0 \\ 0 & 0 & 0 & \boldsymbol{\Gamma}_{deb} \end{bmatrix};\ \overline{\Gamma}_{des} = \begin{bmatrix} \boldsymbol{\Gamma}_{des} & 0 \\ 0 & \boldsymbol{\Gamma}_{des} \end{bmatrix} \\ \boldsymbol{\Gamma}_{rb} = diag(1,1,2);\ \boldsymbol{\Gamma}_{rs} = diag(2,2);\ \boldsymbol{\Gamma}_{deb} = diag(1,1,3,3,3,3);\ \boldsymbol{\Gamma}_{des} = diag(1,3,3,6) \end{gathered} \tag{A5}$$

$$(\mathbf{A}_b, \mathbf{B}_b, \mathbf{D}_b, \mathbf{E}_b, \mathbf{F}_b, \mathbf{H}_b) = \int_{-h/2}^{h/2} \mathbf{C}_b \left(1, z, z^2, f(z), zf(z), f^2(z)\right) \mathrm{d}z$$
$$\overline{\mathbf{C}}_s = \int_{-h/2}^{h/2} \mathbf{C}_s (1 + f'(z))^2 \mathrm{d}z$$
$$(\mathbf{A}_{rb}, \mathbf{B}_{rb}, \mathbf{D}_{rb}) = \int_{-h/2}^{h/2} 2\mu l_1^2 \left(1, f'(z), f'^2(z)\right) \mathbf{I}_{3x3} \mathrm{d}z$$
$$(\mathbf{A}_{rs}, \mathbf{B}_{rs}, \mathbf{D}_{rs}) = \int_{-h/2}^{h/2} 2\mu l_1^2 \left(1, f''(z), f''^2(z)\right) \mathbf{I}_{2x2} \mathrm{d}z$$
$$(\mathbf{A}_{dil}, \mathbf{B}_{dil}, \mathbf{D}_{dil}, \mathbf{C}_{dil}, \mathbf{E}_{dil}) = \int_{-h/2}^{h/2} 2\mu l_2^2 \left(1, z, z^2, f(z), f'(z)\right) \mathbf{I}_{3x3} \mathrm{d}z \tag{A6}$$
$$(\mathbf{F}_{dil}, \mathbf{L}_{dil}, \mathbf{H}_{dil}, \mathbf{O}_{dil}, \mathbf{P}_{dil}) = \int_{-h/2}^{h/2} 2\mu l_2^2 \left(zf(z), zf'(z), f^2(z), f(z)f'(z), f'^2(z)\right) \mathbf{I}_{3x3} \mathrm{d}z$$
$$(\mathbf{A}_{deb}, \mathbf{B}_{deb}, \mathbf{D}_{deb}, \mathbf{C}_{deb}, \mathbf{E}_{deb}) = \int_{-h/2}^{h/2} 2\mu l_3^2 \left(1, z, z^2, f(z), f''(z)\right) \mathbf{I}_{6x6} \mathrm{d}z$$
$$(\mathbf{F}_{deb}, \mathbf{L}_{deb}, \mathbf{H}_{deb}, \mathbf{O}_{deb}, \mathbf{P}_{deb}) = \int_{-h/2}^{h/2} 2\mu l_3^2 \left(zf(z), zf''(z), f^2(z), f(z)f''(z), f''^2(z)\right) \mathbf{I}_{6x6} \mathrm{d}z$$
$$(\mathbf{A}_{des}, \mathbf{B}_{des}, \mathbf{D}_{des}) = \int_{-h/2}^{h/2} 2\mu l_3^2 \left(1, f'(z), f'^2(z)\right) \mathbf{I}_{4x4} \mathrm{d}z$$

$$\mathbf{B}_{b1i} = \begin{bmatrix} N_{i,x} & 0 & 0 & 0 \\ 0 & N_{i,y} & 0 & 0 \\ N_{i,y} & N_{i,x} & 0 & 0 \end{bmatrix};\ \mathbf{B}_{b2i} = -\begin{bmatrix} 0 & 0 & N_{i,xx} & 0 \\ 0 & 0 & N_{i,yy} & 0 \\ 0 & 0 & 2N_{i,xy} & 0 \end{bmatrix};\ \mathbf{B}_{b3i} = \begin{bmatrix} 0 & 0 & 0 & N_{i,xx} \\ 0 & 0 & 0 & N_{i,yy} \\ 0 & 0 & 0 & 2N_{i,xy} \end{bmatrix} \tag{A7}$$
$$\overline{\mathbf{B}}_{si} = \begin{bmatrix} 0 & 0 & 0 & N_{i,x} \\ 0 & 0 & 0 & N_{i,y} \end{bmatrix}$$

$$\mathbf{B}_{rb1i} = \begin{bmatrix} 0 & 0 & N_{i,xy} & \frac{1}{2}N_{i,xy} \\ 0 & 0 & -N_{i,xy} & -\frac{1}{2}N_{i,xy} \\ 0 & 0 & \frac{1}{2}\left(N_{i,yy} - N_{i,xx}\right) & \frac{1}{4}\left(N_{i,yy} - N_{i,xx}\right) \end{bmatrix};\ \mathbf{B}_{rb2i} = \begin{bmatrix} 0 & 0 & 0 & -\frac{1}{2}N_{i,xy} \\ 0 & 0 & 0 & \frac{1}{2}N_{i,xy} \\ 0 & 0 & 0 & \frac{1}{4}\left(N_{i,xx} - N_{i,yy}\right) \end{bmatrix}$$
$$\mathbf{B}_{rs1i} = \frac{1}{4}\begin{bmatrix} -N_{i,xy} & N_{i,xx} & 0 & 0 \\ -N_{i,yy} & N_{i,xy} & 0 & 0 \end{bmatrix};\ \mathbf{B}_{rs2i} = \frac{1}{4}\begin{bmatrix} 0 & 0 & 0 & -N_{i,y} \\ 0 & 0 & 0 & N_{i,x} \end{bmatrix} \tag{A8}$$
$$\mathbf{B}_{1i}^{dil} = \begin{bmatrix} N_{i,xx} & N_{i,xy} & 0 & 0 \\ N_{i,xy} & N_{i,yy} & 0 & 0 \\ 0 & 0 & -N_{i,xx} - N_{i,yy} & 0 \end{bmatrix};\ \mathbf{B}_{2i}^{dil} = \begin{bmatrix} 0 & 0 & -N_{i,xxx} - N_{i,xyy} & 0 \\ 0 & 0 & -N_{i,yyy} - N_{i,xxy} & 0 \\ 0 & 0 & 0 & 0 \end{bmatrix}$$
$$\mathbf{B}_{3i}^{dil} = \begin{bmatrix} 0 & 0 & 0 & N_{i,xxx} + N_{i,xyy} \\ 0 & 0 & 0 & N_{i,yyy} + N_{i,xxy} \\ 0 & 0 & 0 & 0 \end{bmatrix};\ \mathbf{B}_{4i}^{dil} = \begin{bmatrix} 0 & 0 & 0 & 0 \\ 0 & 0 & 0 & 0 \\ 0 & 0 & 0 & N_{i,xx} + N_{i,yy} \end{bmatrix}$$

$$\mathbf{B}_{1i}^{deb} = \begin{bmatrix} \frac{2}{5}N_{i,xx} - \frac{1}{5}N_{i,yy} & -\frac{2}{5}N_{i,xy} & 0 & 0 \\ -\frac{2}{5}N_{i,xy} & \frac{2}{5}N_{i,yy} - \frac{1}{5}N_{i,xx} & 0 & 0 \\ -\frac{1}{5}N_{i,xx} + \frac{4}{15}N_{i,yy} & \frac{8}{15}N_{i,xy} & 0 & 0 \\ \frac{8}{15}N_{i,xy} & -\frac{1}{5}N_{i,yy} + \frac{4}{15}N_{i,xx} & 0 & 0 \\ -\frac{1}{5}N_{i,xx} - \frac{1}{15}N_{i,yy} & -\frac{2}{15}N_{i,xy} & 0 & 0 \\ -\frac{2}{15}N_{i,xy} & -\frac{1}{5}N_{i,yy} - \frac{1}{15}N_{i,xx} & 0 & 0 \end{bmatrix}; \mathbf{B}_{2i}^{deb} = \begin{bmatrix} 0 & 0 & -\frac{2}{5}N_{i,xxx} + \frac{3}{5}N_{i,xyy} & 0 \\ 0 & 0 & -\frac{2}{5}N_{i,yyy} + \frac{3}{5}N_{i,xxy} & 0 \\ 0 & 0 & \frac{1}{5}N_{i,xxx} - \frac{4}{5}N_{i,xyy} & 0 \\ 0 & 0 & \frac{1}{5}N_{i,yyy} - \frac{4}{5}N_{i,xxy} & 0 \\ 0 & 0 & \frac{1}{5}N_{i,xxx} + \frac{1}{5}N_{i,xyy} & 0 \\ 0 & 0 & \frac{1}{5}N_{i,yyy} + \frac{1}{5}N_{i,xxy} & 0 \end{bmatrix}$$

$$\mathbf{B}_{3i}^{deb} = \begin{bmatrix} 0 & 0 & 0 & \frac{2}{5}N_{i,xxx} - \frac{3}{5}N_{i,xyy} \\ 0 & 0 & 0 & \frac{2}{5}N_{i,yyy} - \frac{3}{5}N_{i,xxy} \\ 0 & 0 & 0 & -\frac{1}{5}N_{i,xxx} + \frac{4}{5}N_{i,xyy} \\ 0 & 0 & 0 & -\frac{1}{5}N_{i,yyy} + \frac{4}{5}N_{i,xxy} \\ 0 & 0 & 0 & -\frac{1}{5}N_{i,xxx} - \frac{1}{5}N_{i,xyy} \\ 0 & 0 & 0 & -\frac{1}{5}N_{i,yyy} - \frac{1}{5}N_{i,xxy} \end{bmatrix}; \mathbf{B}_{4i}^{deb} = \begin{bmatrix} 0 & 0 & 0 & -\frac{1}{5}N_{i,x} \\ 0 & 0 & 0 & -\frac{1}{5}N_{i,y} \\ 0 & 0 & 0 & -\frac{1}{15}N_{i,x} \\ 0 & 0 & 0 & -\frac{1}{15}N_{i,y} \\ 0 & 0 & 0 & \frac{4}{15}N_{i,x} \\ 0 & 0 & 0 & \frac{4}{15}N_{i,y} \end{bmatrix} \tag{A9}$$

$$\mathbf{B}_{1i}^{des} = \begin{bmatrix} 0 & 0 & \frac{1}{5}N_{i,xx} + \frac{1}{5}N_{i,yy} & -\frac{1}{5}N_{i,xx} - \frac{1}{5}N_{i,yy} \\ 0 & 0 & -\frac{4}{15}N_{i,xx} + \frac{1}{15}N_{i,yy} & \frac{4}{15}N_{i,xx} - \frac{1}{15}N_{i,yy} \\ 0 & 0 & -\frac{4}{15}N_{i,yy} + \frac{1}{15}N_{i,xx} & \frac{4}{15}N_{i,yy} - \frac{1}{15}N_{i,xx} \\ 0 & 0 & -\frac{1}{3}N_{i,xy} & \frac{1}{3}N_{i,xy} \end{bmatrix}; \mathbf{B}_{2i}^{des} = \begin{bmatrix} 0 & 0 & 0 & -\frac{2}{5}N_{i,xx} - \frac{2}{5}N_{i,yy} \\ 0 & 0 & 0 & \frac{8}{15}N_{i,xx} - \frac{2}{15}N_{i,yy} \\ 0 & 0 & 0 & \frac{8}{15}N_{i,yy} - \frac{2}{15}N_{i,xx} \\ 0 & 0 & 0 & \frac{2}{3}N_{i,xy} \end{bmatrix}$$

$$\mathbf{N}_{1i} = \begin{bmatrix} N_i & 0 & 0 & 0 \\ 0 & N_i & 0 & 0 \\ 0 & 0 & N_i & N_i \end{bmatrix}; \mathbf{N}_{2i} = \begin{bmatrix} 0 & 0 & -N_{i,x} & 0 \\ 0 & 0 & -N_{i,y} & 0 \\ 0 & 0 & 0 & 0 \end{bmatrix}; \mathbf{N}_{3i} = \begin{bmatrix} 0 & 0 & 0 & N_{i,x} \\ 0 & 0 & 0 & N_{i,y} \\ 0 & 0 & 0 & 0 \end{bmatrix} \tag{A10}$$

Data availability

No data was used for the research described in the article.

References

[1] Mindlin RD. Second gradient of strain and surface-tension in linear elasticity. Int J Solids Struct 1965;1(4):417–38.
[2] Lam DCC, Yang F, Chong ACM, Wang J, Tong P. Experiments and theory in strain gradient elasticity. J Mech Phys Solids 2003;51(8):1477–508.
[3] Jamalpoor A, Hosseini M. Biaxial buckling analysis of double-orthotropic microplate-systems including in-plane magnetic field based on strain gradient theory. Compos B: Eng 2015;75:53–64.
[4] Ashoori A, Mahmoodi M. A nonlinear thick plate formulation based on the modified strain gradient theory. Mech Adv Mater Struct 2018;25(10):813–9.
[5] Kandaz M, Dal H. A comparative study of modified strain gradient theory and modified couple stress theory for gold microbeams. Arch Appl Mech 2018;88:2051–70.
[6] Gholami M, Alizadeh M. A quasi-3D modified strain gradient formulation for static bending of functionally graded micro beams resting on Winkler-Pasternak elastic foundation. Sci Iran 2022;29(1):26–40.
[7] Ansari R, Shojaei MF, Mohammadi V, Gholami R, Rouhi H. Size-dependent thermal buckling and postbuckling of functionally graded annular microplates based on the modified strain gradient theory. J Therm Stress 2014;37(2):174–201.
[8] Zhang B, He Y, Liu D, Shen L, Lei J. An efficient size-dependent plate theory for bending, buckling and free vibration analyses of functionally graded microplates resting on elastic foundation. Appl Math Model 2015;39(13):3814–45.
[9] L-y Zhu, L Li, Z-a Li, J-p Shi, W-l Tang, J-q Yang, et al. Design and biomechanical characteristics of porous meniscal implant structures using triply periodic minimal surfaces. J Transl Med 2019;17(1):1–10.
[10] Yuan L, Ding S, Wen C. Additive manufacturing technology for porous metal implant applications and triple minimal surface structures: a review. Bioact Mater 2019;4:56–70.
[11] Hussain I, Al-Ketan O, Renda F, Malvezzi M, Prattichizzo D, Seneviratne L, et al. Design and prototyping soft–rigid tendon-driven modular grippers using interpenetrating phase composites materials. Int J Robot Res 2020;39(14):1635–46.
[12] Yang W, An J, Chua CK, Zhou K. Acoustic absorptions of multifunctional polymeric cellular structures based on triply periodic minimal surfaces fabricated by stereolithography. Virtual Phys Prototyp 2020;15(2):242–9.
[13] Sychov M, Lebedev L, Dyachenko S, Nefedova L. Mechanical properties of energy-absorbing structures with triply periodic minimal surface topology. Acta Astronaut 2018;150:81–4.
[14] Zhang L, Feih S, Daynes S, Chang S, Wang MY, Wei J, et al. Energy absorption characteristics of metallic triply periodic minimal surface sheet structures under compressive loading. Addit Manuf 2018;23:505–15.
[15] Tran P, Peng C. Triply periodic minimal surfaces sandwich structures subjected to shock impact. J Sandw Struct Mater 2021;23(6):2146–75.
[16] Maskery I, Sturm L, Aremu AO, Panesar A, Williams CB, Tuck CJ, et al. Insights into the mechanical properties of several triply periodic minimal surface lattice structures made by polymer additive manufacturing. Polymer 2018;152:62–71.

[17] Simsek U, Arslan T, Kavas B, Gayir CE, Sendur P. Parametric studies on vibration characteristics of triply periodic minimum surface sandwich lattice structures. Int J Adv Manuf Technol 2021;115(3):675–90.
[18] Abueidda DW, Bakir M, RKA Al-Rub, Bergström JS, Sobh NA, Jasiuk I. Mechanical properties of 3D printed polymeric cellular materials with triply periodic minimal surface architectures. Mater Des 2017;122:255–67.
[19] Altintas G. Vibration properties of TPMS based structures. Int J Sci Technol Res 2018;4:27–42.
[20] Kurup M, Pitchaimani J. Aeroelastic flutter of triply periodic minimal surface (TPMS) beams. Compos C: Open Access 2023;10:100349.
[21] Yu S, Sun J, Bai J. Investigation of functionally graded TPMS structures fabricated by additive manufacturing. Mater Des 2019;182:108021.
[22] Viet N, Zaki W. Free vibration and buckling characteristics of functionally graded beams with triply periodic minimal surface architecture. Compos Struct 2021;274: 114342.
[23] Zhang C, Jiang Z, Zhao L, Guo W, Jiang Z, Li X, et al. Mechanical characteristics and deformation mechanism of functionally graded triply periodic minimal surface structures fabricated using stereolithography. Int J Mech Sci 2021;208:106679.
[24] Ejeh CJ, Barsoum I, RKA Al-Rub. Flexural properties of functionally graded additively manufactured AlSi10Mg TPMS latticed-beams. Int J Mech Sci 2022;223: 107293.
[25] Nguyen-Xuan H, Tran KQ, Thai CH, Lee J. Modelling of functionally graded triply periodic minimal surface (FG-TPMS) plates. Compos Struct 2023:116981.
[26] Zhou Z, Ni Y, Tong Z, Zhu S, Sun J, Xu X. Accurate nonlinear buckling analysis of functionally graded porous graphene platelet reinforced composite cylindrical shells. Int J Mech Sci 2019;151:537–50.
[27] Yang J, Wu H, Kitipornchai S. Buckling and postbuckling of functionally graded multilayer graphene platelet-reinforced composite beams. Compos Struct 2017; 161:111–8.
[28] Wang Y, Feng C, Wang X, Zhao Z, Romero CS, Dong Y, et al. Nonlinear static and dynamic responses of graphene platelets reinforced composite beam with dielectric permittivity. Appl Math Model 2019;71:298–315.
[29] Ebrahimi F, Qaderi S. Stability analysis of embedded graphene platelets reinforced composite plates in thermal environment. Eur Phys J Plus 2019;134(7):349.
[30] Gholami R, Ansari R. Large deflection geometrically nonlinear analysis of functionally graded multilayer graphene platelet-reinforced polymer composite rectangular plates. Compos Struct 2017;180:760–71.
[31] Kiani Y, Żur KK. Free vibrations of graphene platelet reinforced composite skew plates resting on point supports. Thin-Walled Struct 2022;176:109363.
[32] Qaderi S, Ebrahimi F, Mahesh V. Free vibration analysis of graphene platelets–reinforced composites plates in thermal environment based on higher-order shear deformation plate theory. Int J Aeronaut Space Sci 2019;20(4):902–12.
[33] Song M, Kitipornchai S, Yang J. Free and forced vibrations of functionally graded polymer composite plates reinforced with graphene nanoplatelets. Compos Struct 2017;159:579–88.
[34] Wang Y, Feng C, Yang J, Zhou D, Liu W. Static response of functionally graded graphene platelet–reinforced composite plate with dielectric property. J Intell Mater Syst Struct 2020;31(19):2211–28.
[35] Pashmforoush F. Statistical analysis on free vibration behavior of functionally graded nanocomposite plates reinforced by graphene platelets. Compos Struct 2019;213:14–24.
[36] Demir Y, Turan F. Stability of porous orthotropic laminated cylindrical panels subjected to linearly varying edge compression based on shear deformation theory. Mech Adv Mater Struct 2024;31(28):10768–81.
[37] Saffari PR, Thongchom C, Saffari PR, Lawongkerd J, Keawsawasvong S, Senjuntichai T. Free vibration of thermally loaded FG-GPLRC nanoplates integrated with magneto-electro-elastic layers in contact with fluid. Int J Struct Stab Dyn 2024;25(11):2550113.
[38] Liang Y, Zhao X, Li Y, Zheng S. Nonlinear thermo-mechanical isogeometric analysis of axially functionally graded porous graphene platelet-reinforced composite arches resting on Winkler–Pasternak foundation. Arch Appl Mech 2025;95(4):88.
[39] Tran KQ, Hoang T-D, Lee J, Nguyen-Xuan H. Three novel computational modeling frameworks of 3D-printed graphene platelets reinforced functionally graded triply periodic minimal surface (GPLR-FG-TPMS) plates. Appl Math Model 2024;126: 667–97.
[40] Do N-T, Dang HT, Tran TT, Du NV, Pham QH. Dynamic response-based isogeometric analysis of graphene platelets-reinforced functionally graded triply periodic minimal surface plates supported by Pasternak foundation. Alex Eng J 2025;110:245–60.
[41] Nguyen NV, Tran KQ, Lee J, Nguyen-Xuan H. Nonlocal strain gradient-based isogeometric analysis of graphene platelets-reinforced functionally graded triply periodic minimal surface nanoplates. Appl Math Comput 2024;466:128461.
[42] Pham QH, Cuong-Le T. Nonlocal forced vibration analysis of graphene platelets-reinforced functionally graded triply periodic minimal surface nanoplates embedded in elastic foundation using Reddy-IGA. Mech. Based Des. Struct. Mach. 2025:1–27.
[43] Thai S, Thai H-T, Vo TP. Nguyen-Xuan H. Nonlinear static and transient isogeometric analysis of functionally graded microplates based on the modified strain gradient theory. Eng Struct 2017;153:598–612.
[44] Thai CH, Ferreira AJM. Nguyen-Xuan H. Isogeometric analysis of size-dependent isotropic and sandwich functionally graded microplates based on modified strain gradient elasticity theory. Compos Struct 2018;192:274–88.
[45] Farzam A, Hassani B. Size-dependent analysis of FG microplates with temperature-dependent material properties using modified strain gradient theory and isogeometric approach. Compos. B: Eng. 2019;161:150–68.
[46] Nguyen NV, Tran KQ, Phung-Van P Lee J, Nguyen-Xuan H. An isogeometric analysis of functionally graded triply periodic minimal surface microplates. Aerosp Sci Technol 2023;137:108270.
[47] Roberts AP, Garboczi EJ. Elastic moduli of model random three-dimensional closed-cell cellular solids. Acta Mater 2001;49(2):189–97.
[48] Gibson LJ. Cellular Solids. MRS Bull 2003;28(4):270–4.
[49] Affdl JH, Kardos J. The Halpin-Tsai equations: a review. Polym Eng Sci 1976;16(5): 344–52.
[50] De Villoria RG, Miravete A. Mechanical model to evaluate the effect of the dispersion in nanocomposites. Acta Mater 2007;55(9):3025–31.
[51] Ke L-L, Yang J, Kitipornchai S. Nonlinear free vibration of functionally graded carbon nanotube-reinforced composite beams. Compos Struct 2010;92(3):676–83.
[52] Nguyen NV, Tran KQ, Phung-Van P Lee J, Nguyen-Xuan H. An isogeometric analysis of functionally graded triply periodic minimal surface microplates. Aerosp Sci Technol 2023:108270.
[53] Senthilnathan N, Lim S, Lee K, Chow S. Buckling of shear-deformable plates. AIAA J 1987;25(9):1268–71.
[54] Lam DC, Yang F, Chong A, Wang J, Tong P. Experiments and theory in strain gradient elasticity. J Mech Phys Solids 2003;51(8):1477–508.
[55] Hughes TJ, Cottrell JA, Bazilevs Y. Isogeometric analysis: CAD, finite elements, NURBS, exact geometry and mesh refinement. Comput Methods Appl Mech Eng 2005;194(39–41):4135–95.